UNVIERSITY OF CALIFORNIA SAN DIEGO

Anisotropic Wetting Property of Superhydrophobic Surfaces and Electrokinetic Flow on Liquid-Filled Surfaces

A Dissertation submitted in partial satisfaction of the
requirements for the degree
Doctor of Philosophy

in

Engineering Sciences (Mechanical Engineering)

by

Bei Fan

Committee in charge:

Professor Prabhakar R. Bandaru, Chair
Professor Shengqiang Cai
Professor James R. Friend
Professor Yu Qiao
Professor David Saintillan

2019

The Dissertation of Bei Fan is approved, and it is acceptable in quality and form for publication on microfilm and electronically:

_____

_____

_____

_____

_____

Chair

University of California San Diego

2019

TABLE OF CONTENTS

LIST OF FIGURES

LIST OF TABLES

ACKNOWLEDGEMENTS

I would like to acknowledge Professor Prabhakar Bandaru for his support as the chair of my committee and in my research endeavors. I'm grateful to his patience in my Ph. D period and his valuable help and advice on my career development. I would also like to thank my lab mates for their help in my research. I would also like to acknowledge my committee member who provided precious suggestions in my research and support for my career.

I would like to thank my parents for their support and patience in my Ph. D studies. I would also like my thank my friends for their help both in my study and life.

Chapter 2, in full, is a reprint of the materials as it appears in Fan, B. and Bandaru, P.R., Anisotropy in the hydrophobic and oleophobic characteristics of patterned surfaces, Appl. Phys. Lett, 111, 261603, 2017. The dissertation author was the primary investigator and author of this paper.

Chapter 3, in full, is a reprint of the materials as it appears in Fan, B., Bhattacharya, A. and Bandaru, P.R., Enhanced voltage generation through electrolyte flow on liquid-filled surfaces, Nature Communications, 9, 4050, 2018. The dissertation author was the primary investigator and author of this paper.

Chapter 4, in full, is a reprint of the materials as it appears in Fan, B. and Bandaru, P.R., Modulation of streaming potential and slip characteristics in electrolyte flow over liquid-filled surfaces, Langmuir, 2019, 35, 18, 6203 – 6210.The dissertation author was the primary investigator and author of this paper.

Chapter 5, in full, is a reprint of the materials as it appears in Fan, B. and Bandaru, P.R., Tensorial modulation of electrokinetic streaming potentials on air and liquid filled surfaces, Langmuir, 2019, 35, 46, 14812 – 14817. The dissertation author was the primary investigator and author of this paper.

VITA

2015	Bachelor of Engineering, University of Science and Technology of China
2016	Master, University of California San Diego
2019	Doctor of Philosophy, University of California San Diego

PUBLICATIONS

Fan, B. and Bandaru, P.R., Tensorial modulation of electrokinetic streaming potentials on air and liquid filled surfaces, *Langmuir*, 2019, 35, 46, 14812 – 14817.

Fan, B. and Bandaru, P.R., Modulation of streaming potential and slip characteristics in electrolyte flow over liquid-filled surfaces, *Langmuir*, 2019, 35, 18, 6203 – 6210.

Fan, B., Bhattacharya, A. and Bandaru, P.R., Enhanced voltage generation through electrolyte flow on liquid-filled surfaces, *Nature Communications*, 9, 4050 (2018).

Fan, B. and Bandaru, P.R., Anisotropy in the hydrophobic and oleophobic characteristics of patterned surfaces, *Appl. Phys. Lett*, 111, 261603 (2017).

ABSTRACT OF THE DISSERTATION

Anisotropic Wetting Property of Superhydrophobic Surfaces and Electrokinetic Flow on Liquid-Filled Surfaces

by

Bei Fan

Doctor of Philosophy of Engineering Sciences (Mechanical Engineering)

University of California San Diego, 2019

Professor Prabhakar R. Bandaru, Chair

Understanding the wetting property of rough surface is critical in guiding droplets and novel superhydrophobic surface design. The Cassie-Baxter model and Wenzel model are always used to describe the totally non-wetting and completely wetting states, however, there were few discussions about the intermediate state. Through measuring the contact angles of groove patterned surfaces in different groove orientations, the anisotropic wetting properties of groove patterned superhydrophobic surface were investigated. The degree of water penetration into the grooves was experimentally observed and it was found that the degree of water penetration was different with groove orientations, which would affect the corresponding contact angle. Besides guiding droplets, superhydrophobic surfaces are also very important in microfluidic due to their ability to generate fluid slip and flow enhancement. After a deeper understanding

of the wetting property of groove patterned superhydrophobic surface, I further investigated its important role in microfluidics. In this dissertation, I mainly focus on electrokinetics on groove patterned surface and liquid-filled slippery surfaces, a new kind of surface by filling low surface tension oil into the interstices of groove patterned surfaces. I experimentally measured the streaming potential on flat parylene surface, air-filled groove patterned surface and liquid-filled surfaces and compared their effects in streaming potential enhancement. The liquid-filled surfaces were shown to be able to enhance the generated streaming potential due to its slippery property and liquid-oil interface charges. As the electrokinetic on liquid-filled surfaces is a new phenomenon, the underlying physics is still not clear. I further investigated the influences of filled oil properties and groove orientation on streaming potentials and fluid slip. Oils with different densities, viscosities, dielectric constant, conductivities and surface tensions were filled into the interstices of groove patterned surfaces to make different types of liquid-filled surfaces. The streaming potentials on liquid-filled surfaces with different oils were experimentally measured. An empirical relationship between streaming potential and oil properties was found and the effects of electrical properties, such as interface charge density and dielectric constant of filled oil, on fluid slip were also studied. Finally, the groove orientation was varied to study the tensorial effects on streaming potential. Through both streaming potential measurement and theoretical analysis, it was found that the streaming potential at 45° was always smaller than the arithmetic mean of those at 0° and 90°, and the pressure gradient in the transvers direction generated by tensorial effects was important in the streaming potential modification. My work will be important in guiding droplets, flow patterning, lab-on-chip devices and the development of electrokientic based power sources.

Chapter 1 Introduction

1.1 Wetting models on rough surface

When a water droplet contacts with a solid surface, there exists a thermodynamic equilibrium state of the three phases that are liquid phase, vapor phase and solid phase and form a contact angle (θ_c) as shown in Figure 1.1. Through the force balance at the contact line or triple line, the contact angle can be calculated using the Young equation[1]:

$$\gamma_{SA} - \gamma_{SL} - \gamma_{LA}cos\theta_c = 0 \tag{1.1}$$

γ_{SA} is the solid-air interface energy, γ_{SL} is the solid-liquid interface energy and γ_{LA} is the liquid-air interface energy.

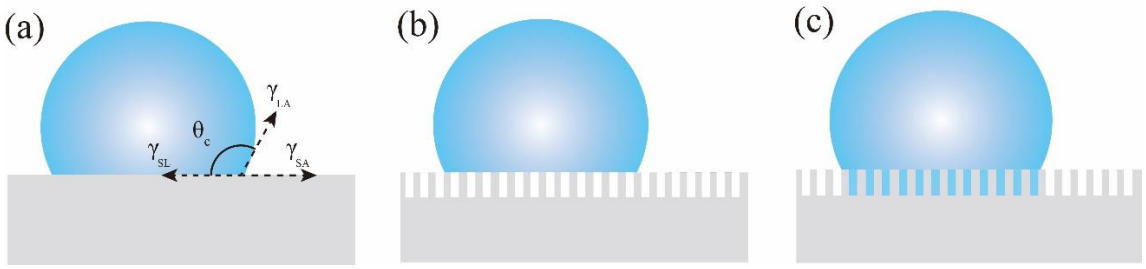

Figure 1.1 (a) Liquid droplet on flat surface and the formation of contact angle, (b) Cassie and (c) Wenzel state on rough surface.

When the liquid droplet contacts with a rough surface, the Cassie and Wenzel model are usually used to describe the wetting state of the substrate. The Cassie state, indicating in Figure 1.1(b), describes the completely non-wetting state at which the liquid droplet will stay above the pattern. The Wenzel state in Figure 1.1(c) describes the totally wetting state and the liquid will completely fill into the interstices of the rough surface.

1.4 Electrokinetics

When electrolyte contacts with a solid surface, there will form an electrochemical double layer (EDL) structure due to the mismatch of dielectric constant (ε). Generally, the electrolyte with a larger dielectric constant flows over a material with smaller dielectric constant, the solid surface will be negatively charged[2]. At the electrolyte-solid interface, the negative charged solid interface will attract positive counter-ions near the solid surface and form the doubly layer structure. The first layer will be stern layer which consists fixed positive ions adhered to the solid surface and those positive ions can not move with electrolyte. The second layer is diffuse layer which contains mostly positive ions which can move with the fluid flow. The characteristic thickness of EDL is defined as Debye length λ_D as indicated in Figure 1.2. The $\lambda_D = \sqrt{\frac{\varepsilon_0 \varepsilon_r k_B T}{2N_A (ze)^2 I}}$, ε_0 is the dielectric constant of free space, ε_r is the relative dielectric constant of the electrolyte, k_B is Boltzmann constant, T is the temperature, N_A is Avogadro's number, z is the number of charge of the ion, e is the elementary electron charge and I is the concentration, the $\lambda_D \sim \frac{9.6}{\sqrt{I}}$ (the units of λ_D and I are nm and mM) for electrolytes composed of ions with single charge. Under a pressure driven flow, say the pressure drop is $\Delta P = P_2 - P_1$, as indicated in Figure 1.2, the positive ions in the diffuse layer will move with the fluid and accumulate at the right end of the channel, due to the ion accumulation, an imbalance between the ion concentration is built up between the ends of the channel which can induce a potential difference termed as streaming potential[2]. The generated streaming potential, V_s, is related to the dielectric constant ε (=$\varepsilon_r \varepsilon_0$), viscosity η, conductivity σ, the zeta potential ζ of the surface and the pressure drop ΔP through[2]:

$$V_s = \frac{\varepsilon \zeta}{\eta \sigma} \Delta P \tag{1.2}$$

The derivation of Eqn. 1.2 is based on the following assumptions[2]: (a) negligible surface conductivity, (b) thin EDL, (c) the Debye-Huckel assumption that the wall potential is of the order of ~ 26 mV (=$k_B T/e$, where k_B is the Boltzmann constant ~ 8.6×10^{-5} eV/K, T is the temperature at ~ 300 K in

the ambient, and e is the elementary electronic charge = 1.602×10^{-19} C). As electrokinetic flow can convert mechanical energy to electricity and there is no moving parts in the structure, it is promising to be developed as microchannel battery[3], the power sources for MEMS system and wearable devices.

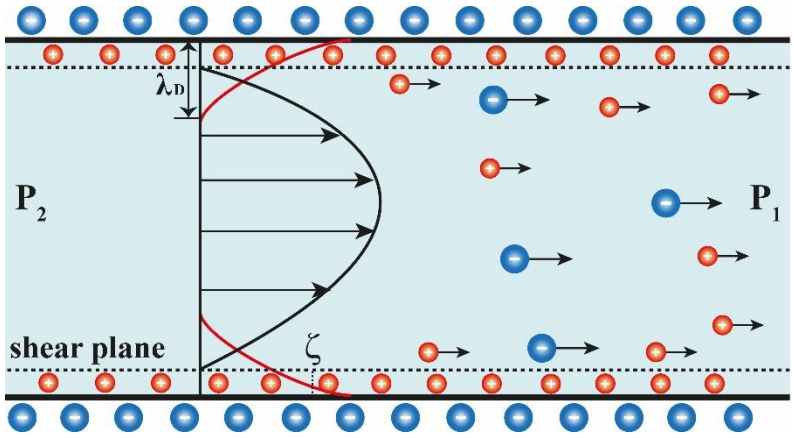

Figure 1.2 Electrokinetic flow on a flat surface under a pressure drop ΔP ($=P_2 - P_1$). ζ is the zeta potential which is the potential at the shear plan where fluid starts to move.

1.3 Motivation

Superhydrophobic surfaces which are inspired by lotus leaf and other plant leaves that can not get wet by water are important in both static and dynamic fluid phenomena and have essential practical applications, such as self-clean surface, anti-icing, oil-water separation and drag reduction[4]. To make superdydrophobic surfaces, the traditional method is to make micro/nano scale roughness that will trap air to increase the water contact angle and decrease the tendency of the binding of water to the surface. The wetting property of water on rough surfaces are important in superhydrophobic design. As discussed previously, the Cassie model and Wenzel model are usually used to describe the wetting status of liquid droplet on rough surface. However, there are other conditions that these two models don't consider. For example, both of these two models don't consider the effect of anisotropic property of the roughness on the wetting property. Besides, these two models only describe the two extreme wetting states that are completely wetting and non-wetting states, and there were few discussions abut the intermediate wetting state between these two models. To have a better understanding of the liquid wetting states on rough

surfaces, more work should be done to consider the anisotropic property of the superhydrophobic surface and the partial wetting state to make modifications of current Cassie and Wenzel model.

Besides studying the static liquid wetting on superhydrophobic surface, my work also extended to the continuous and dynamic flow on superhydrophobic due to the important role of superhydrophobic surface in fluid drag reduction and flow enhancement. In electrokinetic field, traditional researches were mainly on flat surface which introduced non-slip boundary condition at the electrolyte-solid interface and yielded low streaming potential[3], which limited the applications of electrokinetic as practical power sources. Then it was proposed that using superhydrophobic surface can introduce fluid slip for streaming potential enhancement[5]. Since the electrical potential decays away from the surface, the further the shear plane is from the substrate boundary the smaller the equivalent ζ and the obtainable V_s. One possible method to enhance the ζ is then to introduce fluid slip at the substrate surface, where the shear plane is moved as close as possible to the substrate. In this case, the zero velocity boundary condition at the surface (y=0) is replaced with a Navier slip condition: u_s (y=0)= $b\frac{\partial u\,(y=0)}{\partial y}$) with b as the slip length (a length below the surface at which the fluid effectively has a zero velocity)[6,7]. The $\zeta$is modified by the introduction of the Navier condition to[8]:

$$\zeta = \psi_o\left(1 + \frac{b}{\lambda_D}\right) \tag{1.3}$$

Hence, a larger slip (implying a larger b) relative to a λ_D for a given solution (with a fixed ε, σ and η could be beneficial in harnessing large V_s – through a closer coupling of the fluid velocity profile to the charged double layer. In this context, it was previously indicated[9] that relatively large values of b of the order of ~ 6 mm may indeed be obtained in superhydrophobic surfaces fabricated through a roll-to-roll processing methodology[10]. As $\lambda_D \sim \frac{9.6}{\sqrt{I}}$, λ_D is around 9.6 nm with 1 mM NaCl, and a consequent b/λ_D of ~ 625, one may be led to expect up to three orders of magnitude larger λ_D. However, there have been theoretical suggestions that the superhydrophobic surfaces may not yield the predicted degree enhancement due to the non-charged liquid-air interfaces introduced by superhdrophobic surfaces[11]. Most of the work on

electrokinetics on superhydrophobic surfaces was theoretical and computational analysis, experimental efforts are necessary to investigate the practical situation. In my dissertation, I will also mainly focus on the experimental study on electrokinetics on superhydrophobic surfaces and will also come up with the solution to streaming potential enhancement.

Chapter 2 Anisotropy in the hydrophobic and oleophilic characteristics of patterned surfaces

2.1 Abstract

A significant difference in the wetting angles of water and oil was observed on patterned substrates, combining interstitial spaces along with hydrophobic solid surfaces, as a function of orientation. The difference was ascribed to a modification of the liquid – interstice interfacial surface energy, due to different degrees of penetration of the liquid. A roughness metric, related to the ratio of the areas related to the extent of which the liquid infiltrates the interstice to the geometrically determined area is proposed. The study has implications in modulating surface slip behavior and would be of importance in guiding liquid droplets, *e.g.*, in electrophoresis.

2.2 Introduction

The extent of wettability of a surface is dependent on the underlying substrate surface energies (γ). Considering the substrate-wetting liquid energy (γ_{SL}), the substrate-ambient energy (γ_{SA}), and the liquid - ambient (*e.g.*, air) energy (γ_{LA}), two related well-known parametric measures[1] are the spreading parameter, *S*, and the contact/wetting angle: θ - determined through the Young relation, *i.e.*,

$$S = \gamma_{SA} - (\gamma_{SL} + \gamma_{LA}) \tag{2.1a}$$

$$\theta = \cos^{-1}[\,(\gamma_{SA} - \gamma_{SL})/\,\gamma_{LA}] \tag{2.1b}$$

The extension to predict the wetting behavior of rough or patterned surfaces has been done through the Cassie-Baxter/*fakir* model: Figure 2.1(a) or the Wenzel (W) model: Figure 2.1(b), which broadly deal with two extremes related to complete exclusion (/inclusion) of the interstices in the solid substrate by the

liquid, respectively. In this letter, we investigate the plausible intermediate regime, *i.e.*, Figure 2.1(c), where there would be partial liquid penetration into patterned substrates: Figure 2.1(d). The parameters of relevance in the Cassie-Baxter and Wenzel models are the respective area fractions of the interstice surface area (ϕ_I) and the solid surface area (ϕ_s), where $\phi_I + \phi_s = 1$, and a somewhat arbitrarily defined roughness parameter: r, as the ratio of the total surface area to the projected/apparent surface area, which would of course depend on the measurement scale. For instance, the Cassie-Baxter model relates the *overall* wetting angle (θ_{net}) to the wetting angle on the air in the interstice (*i.e.*, θ_{int}) and that in the constituent solid (*i.e.*, θ_{sol}) as:

$$\text{Cos}\,(\theta^{F}_{\text{net}}) = \phi_I\,\text{Cos}\,(\theta_{\text{int}}) + \phi_s\,\text{Cos}\,(\theta_{\text{sol}}) \tag{2.2a}$$

Alternately, the Wenzel model indicates a roughness (r) related θ^{W}_{net}, through:

$$\text{Cos}\,(\theta^{W}_{\text{net}}) = r\,\text{Cos}\,(\theta_{\text{sol}}) \tag{2.2b}$$

Per recommendations[12] on the proper use of Eqn. 2.2, we did not assume that the liquid-vapor interface was smooth, and consider liquid penetration into the troughs of the rough surface[13]. An effective medium approach (EMA)[9,10] was implicitly assumed to average the water penetration, whereby the extent of the wetting liquid is much larger compared to the underlying texture, and the perturbations to the liquid drop in the interstice could be considered small.

However, a major issue is that these models do not explicitly consider the anisotropy of the underlying substrate texture. The wetting angle related to the placement of a liquid drop (say, of radius, R ~ 0.3 cm) on a patterned surface (*e.g.*, with 20 μm (=w) ridges, with a $\phi_I = 0.5$) would not be expected, through use of the *fakir* and the Wenzel models to be a function of the orientation of the ridges. However, experimentally we did notice a change, with a larger contact angle when the drop would be translated perpendicular to the ridges compared to an orientation parallel to the ridges: Figure 2.2. The two contact angles imply differing radii of curvature for the impregnated liquid parallel and perpendicular to the ridges[1].

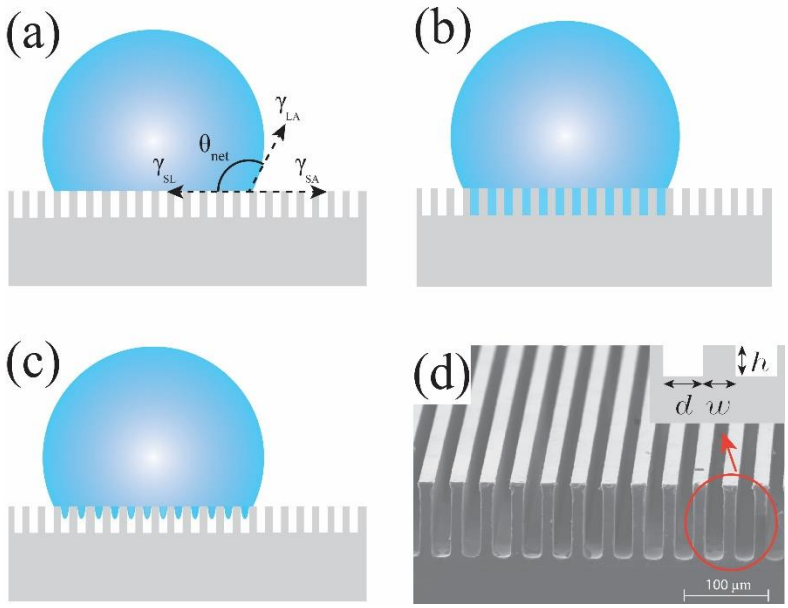

Figure 2.1 Schematic images of the wetting behavior, as indicated through the (a) Cassie-Baxter based fakir model, corresponding to the total absence of impregnation of the interstices by the liquid state, and the (b) Wenzel model, corresponding to the total impregnation by the liquid. I discuss here (c) the intermediate regime, corresponding to partial penetration of the interstices, (d) SEM image of the morphology of the ridged surfaces used for the experiments.

Much previous work on the anisotropy of wetting on textured surfaces[14] has not quantitatively estimated the penetration of liquid into interstices[15]. Measurements on sub-micron scale triangular grooves indicated[16] a state where the water completely penetrates the grooves. It was also discussed[17] that a water droplet may be suspended on patterns (modified with hydrophobic coatings[18]) and does not directly contact the substrate. Along with contact angle hysteresis[19], a proposal that the contact angle decreases as penetration progresses was posited[12]. A related aspect of interest concerns the wetting dynamics, *e.g.*, in low Reynolds number (*Re*) flow. The *fakir* and the Wenzel models are often implicitly assumed in fluid flow[20] for understanding the efficacy of hydrophobic/super-hydrophobic surfaces in reducing fluid drag and inducing slip[21], through reduced shear stress at the moving liquid-air interface. It is then the aim of this paper to examine the influence of anisotropy related to the substrate[22] on the wetting characteristics in static and quasi-static scenarios and lay out the physical rationale behind liquid penetration into the grooves.

2.3 Methods

The tested Parylene-C coated patterned surfaces (on Si substrates) were patterned through standard photolithography. Briefly, coated photoresist on a Si wafer (*n*-type, <110>, and thickness of 500 μm) was patterned, developed and subject to reactive ion etching (RIE) to a trench depth of about 95 μm. The photoresist was then removed and the surface was coated with 1 μm thick Parylene-C. The ridged pattern surface morphology is shown in Figure 2.1(d). The average width (w) and height (h) was ~ 18 μm and ~ 95 μm, respectively, at a distance (d) of 18 μm. We define an interstice fraction: ϕ_I, as the ratio [$= d/(d + w)$], with distances measured through scanning electron microscopy. Two different substrate patterns, lithographically designed for $\phi_I = 0.5$ and $\phi_I = 0.75$, were used. To probe the related anisotropic wetting characteristics, a liquid drop (*i.e.*, 10 μL water, with γ_{LA} of 72.8 mJ/m^2, and 3 μL oil: Krytox® GPL104[23], with γ_{LA} of 18 mJ/m^2) was placed on the Parylene-C coated patterned substrates (using a reported[24] γ_{SV} of 46.2 mJ/m^2), and the contact angles observed in two orthogonal orientations at 20℃ using Ramé-Hart Model 190 Contact Angle Goniometer. For comparison, the contact angle of water drops on the Parylene-C coated substrate (flat and unpatterned) was ~ 94.6^0, with a corresponding γ_{SL} of 51 mJ/m^2 estimated through Eqn. 2.1(b). Detailed contact angle measurements as a function of orientation are indicated through Figure 2.2 and listed in Table 2.1.

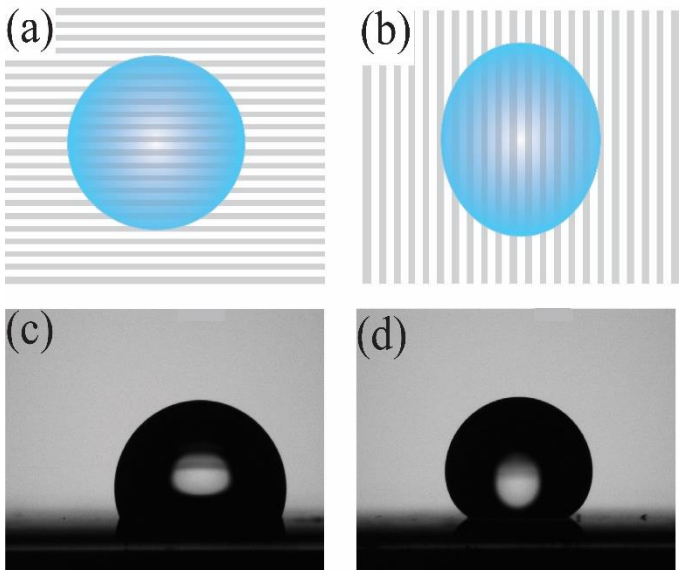

Figure 2.2 Schematics of the top views of a water droplet, on a ridged surface, (a) parallel, and (b) perpendicular, to the ridges. (c) and (d) indicate the corresponding edge-on shapes, respectively.

Table 2.1 The measurements of the contact angle, as a function of the orientation of the ridges. The values in the brackets indicate the corresponding γ_{SL} (= $\gamma_{SL,\,mod}$), in units of mJ/m^2.

		$\phi_s = 0.5$	$\phi_s = 0.25$
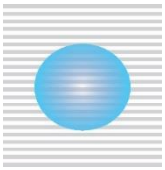	→	111.3° (*72*)	124.9° (*87*)
	↑	147.0° (*107*)	148.5° (*108*)

2.4 Results and Discussions

We denote the *S-L* energies on the patterned surfaces as $\gamma_{SL,mod}$, as *modified* from the values obtained from those on unpatterned Parylene-C coated surfaces. The shapes of the droplets were broadly elliptical, with major axis along the ridge/groove, indicative of macroscopic preferential wetting in this direction. In all cases, the underlying pattern texture enhanced the degree of hydrophobicity, compared to the planar substrate, as indicated by an increase of the wetting angle to greater than 94.6^0. It was noted that the contact angles on the patterned surfaces differ significantly, *e.g.*, by ~ 36^0, (the difference between 147^0 in the

perpendicular orientation *vs.* the 111^0 in the parallel direction) and correlated to the variation in the estimated γ_{SL} (= $\gamma_{SL,\ mod}$) from ~ 107 mJ/m^2 to ~ 72 mJ/m^2.

Generally, when a liquid drop is placed on a patterned surface a small deflection/bowing (δ) of the liquid into the interstices (*I*) is expected based on gravitational considerations[1]: Figure 2.1(c). We consider the surface energy related to the liquid over the interstices as γ_{LI}, *e.g.*, $\gamma_{LI} = \gamma_{LA}$, if the interstice is mostly air (*A*). Here, for a liquid drop of radius *R*, and an interstitial length of *d*, from elementary geometrical considerations, $\delta \sim d^2/8R$. Such deflection is also favored on energetic considerations[25], when γ_{LI} is smaller/comparable to the γ_{SL}. However, considering gravitational forces in addition to surface tension, δwould be proportional to R^3/l_c^2, and the lateral spread (l_{spread}) on the substrate would be proportional to R^2/l_c where l_c (=$\sqrt{\gamma/\rho g}$) is the capillary length, with ρ as the liquid density and *g* the acceleration due to gravity. Consequently, a larger δ or l_{spread} would be favored by a larger/heavier drop and a smaller γ. Then, for a given drop size, the drop infiltrates into the interstice or spreads to lower the net γ. For a large liquid drop on top of a patterned surface, where $R >> w$ and *d*, the net γ, could be formulated through:

$$\gamma_{SL,\ mod} = \phi_s\, \gamma_{SL} + \phi_I^{'}\, \gamma_{LI} \qquad (2.3)$$

Here, $\phi_I^{'}$ is related to the extent to which the liquid penetrates the interstice and may not necessarily be equal to the geometrically patterned ϕ_I. While we designed our patterns: see Figure 2.1(d), with a ϕ_I (=ϕ_s) = 0.5, a smaller ϕ_{LI} (/ ϕ_{LA}) would implicate a larger $\phi_I^{'}$ when other parameters in Eqn. 2.3 are fixed. The computed $\gamma_{SL,mod}$ would then be a better metric to estimate the spreading (*S*) instead of the γ_{SL}.

A measure of drop spreading[26] could occur due to a very small pressure gradient, additional to the l_{spread}. When a liquid drop is moved *parallel* to the direction of the ridges, a given unit of the drop is constantly in contact with the underlying solid *or* interstitial region, during the entire trajectory of the motion. However, when the liquid drop is moved perpendicular to the direction of the ridges, the drop unit alternates contact between the underlying solid *and* the interstitial region. Consequently, in the latter case, the moving liquid drop does not benefit from penetrating further into the interstice, as in the former situation.

It would also be expected that a larger air fraction would increase the penetration and further decrease the extent of wetting on top of the patterned surface, manifesting a larger contact angle: Table 2.I. It is pertinent to note that that such impregnation of the liquid into the interstices yields an overall lower macroscopic wetting of the surface of the patterned substrate[27].

Using Eqn. 2.3, with a computed $\gamma_{SL,\,mod}$ of ~ 72 mJ/m^2 (from Table 2.1), ϕ_s = 0.5, γ_{SL} of 51 mJ/m^2, and γ_{LI} ~ 72.8 mJ/m^2, we obtain a $\phi_I^{'}$ of 0.64: Table 2.2(a). Alternately, with $\gamma_{SL.\,mod}$ of ~ 107 mJ/m^2, and ϕ_s = 0.5, $\phi_I^{'}$ is ~ 1.12: Table 2.2(a). It is to be noted that as $\gamma_{LI} > \gamma_{SL}$, the liquid would be in intimate contact with the solid surface. Then, the ϕ_s and the related γ_{SL} would not change and be equal to the geometrical/patterned value. The solid-liquid interfacial area could then be essentially considered flat. In both cases, the obtained $\phi_I^{'}$ is greater than the patterned ϕ_I of ~ 0.5. The corresponding $\phi_I^{'}$ values, with a ϕ_s (or a ϕ_I of ~ 0.75) of ~ 0.25, were 1.02 and 1.31 – see Table 2.2(a), for the parallel and perpendicular orientation, respectively. Generally, spread of liquid into the groove would be expected to since γ_{SL} (~ 51 mJ/m^2) is less than γ_{LI} (~ 73 mJ/m^2); this would be in addition to the gravity induced penetration into the interstice.

Table 2.2 The values of the fraction: $\phi_I^{'}$, corresponding to the extent to which the liquid penetrates the interstices of the ridged surfaces, for **(a)** water, and **(b)** oil, as estimated from Eqn. 2.3.

(a)		$\phi_s = 0.5$	$\phi_s = 0.25$
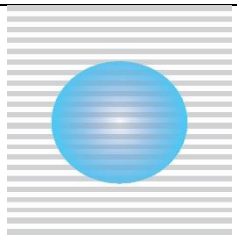	→	0.64	1.02
	↑	1.12	1.31

(b)		$\phi_s = 0.5$
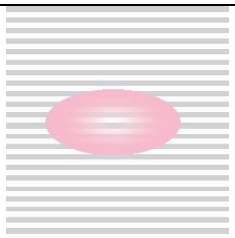	→	0.80
	↑	0.90

Correlating the contact angle measurements in Table 2.1 and the corresponding $\phi_I^{'}$ in Table 2.2(a), we can find that larger water penetration will result in larger $\phi_I^{'}$ and contact angle, and the anisotropy of wetting angles can be attributed to the different degrees of water penetration in different directions. We also directly observe water penetration via confocal microscopy (using a Photron FASTCAM camera): Figure 2.3 and inset. The side-view images, on the bottom left and right of Figure 2.3(b) indicate both non-uniform and partial penetration of the liquid (red dotted lines), as well as full penetration into the interstices, respectively. Our studies preclude evaporation related considerations[28].

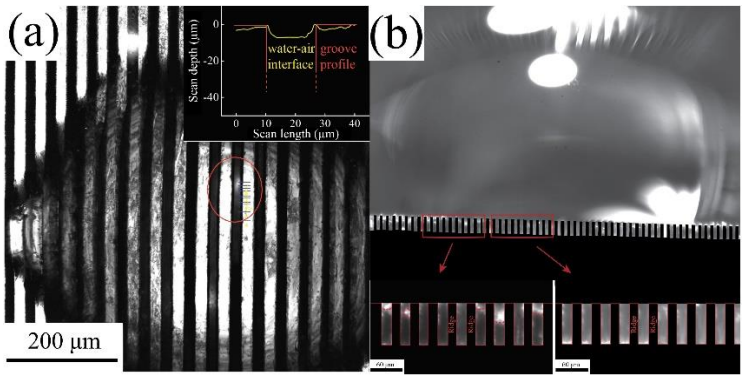

Figure 2.3 (a) Confocal microscopy imaging of a water drop indicates a penetration of liquid into the interstices, of ~ 6 μm as indicated in the inset. The red circle relates to the scan profile of the inset, where the vertical axis is related to the depth of the interstice, while the horizontal axis represents the distance along the interstices, above the patterned surface, (b) The side view of a water drop placed on the patterned substrate. The bottom left inset indicates the presence of water (partial penetration) in the interstices, through the reflecting contrast (from the white patches encompassed by the dotted red lines) and corresponding to the scan profile in the inset of (a). The bottom right inset indicates the infiltration of water (full penetration) into the interstices.

The obtained $\gamma_{SL.\,mod}$ values, together with the degree of penetration of the liquid into the interstices, are intermediate to the solid substrate surface energies (~ 46.2 mJ/m^2) and the summation of the surface energies of the solid substrate and the liquid of ~ 119 mJ/m^2 (= 72.8 mJ/m^2 + 46.2 mJ/m^2), where water was completely penetrating the interstices and tending to avoid the top solid substrate. The anisotropic tendencies in the underlying substrate modulate the extent of wetting/hydrophobic character.

We additionally tested the influence of anisotropy through the placement of Krytox® GPL104 oil on the patterned substrates, with a patterned ϕ_s of 0.5. It was noted that the contact angles parallel and perpendicular to the ridges, was ~ 21.0° and ~ 30.1° respectively. For reference, the contact angle of the oil drop on the unpatterned Parylene-C coated surface was ~ 24.1°, implying a γ_{SL} of 29.6 mJ/m^2, from Eqn. 2.1(b). While the smaller angles indicate a greater oleophilic character for the patterned surfaces, we estimate from Eqn. 2.3, correspondingly higher $\phi_I^{'}$ of ~ 0.8 and ~ 0.9, respectively, as in Table 2.2(b) – indicating again an area enhancement of the oil in the interstice. Contrasting the time-dependent behavior of the water and the oil on the patterned surface: Figure 2.4, while the shape of water did not change much

with time with little spreading, the oil drop spreads along and into the grooves quickly. A film propagates in advance of the oil drop indicating the enhanced oleophilic character due to the ridges.

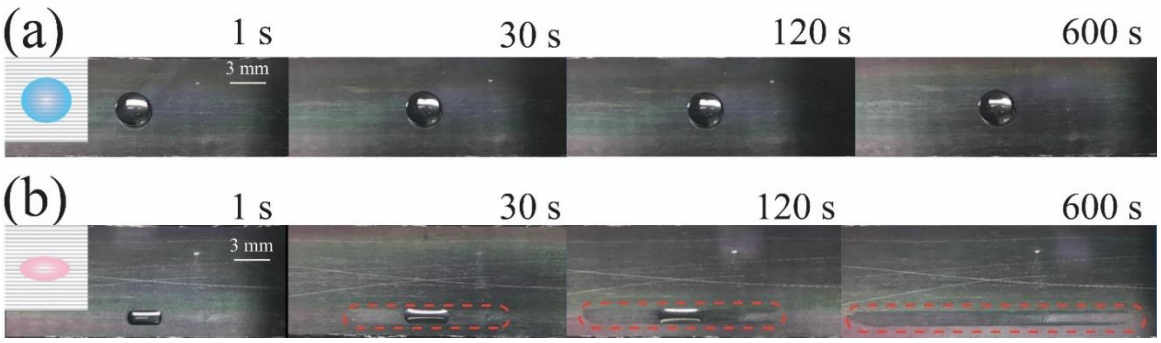

Figure 2.4 The time-dependent spreading of (a) water and (b) Krytox GPL104 oil, on the ridged surface. While the shape of the water drop was relatively stable, the oil drop spreads quickly into the grooves, with a film (outlined in a dotted red line) advancing ahead of the drop.

2.5 Conclusion

Based on the results of our measurements and analyses, it is concluded that the anisotropy of wetting is related to the liquid penetration, where a larger effective air fraction implies larger penetration, yielding a larger contact angle. In most studies[29] related to the influence of patterned surfaces on inducing hydrophobic behavior, the degree of liquid penetration into the interstices has not been much considered[6]. The ratio of the estimated $\phi_I^{'}$ to the ϕ_I (which may be larger or smaller than unity) would enable the definition of a roughness metric, in contrast with the traditional[1] definition: Eqn. 2.2(b). We have indicated that a larger penetration, with a larger interfacial area/contact angle and lower shear would be of significance in modulating hydrophobic and surface slip behavior. The concomitant traversal direction dependent penetration of the liquid into the interstices may also be related to the system size as well as a shear-dependent effective slip length[30]. Related considerations would also be of importance in guiding liquid droplets, *e.g.*, in electrophoretic applications[31], the design of drag-reducing super-hydrophobic surfaces[6,21], *etc.* Future work would focus on the study of liquid flow dynamics as a function of the degree of anisotropy of the underlying patterned surfaces.

2.6 Acknowledgement

This chapter, in full, is a reprint of the materials as it appears in Fan, B. and Bandaru, P.R., Anisotropy in the hydrophobic and oleophobic characteristics of patterned surfaces, Appl. Phys. Lett, 111, 261603, 2017. The dissertation author was the primary investigator and author of this paper. The authors are grateful for support from the National Science Foundation (NSF: CMMI 1246800 and CBET 1606192). We also appreciate the assistance of Prof. James Friend, Shuai Zhang, and Dr. Jonathan Yu for help with imaging and confocal microscopy.

Chapter 3 Enhanced voltage generation through electrolyte flow on liquid-filled surfaces

3.1 Abstract

The generation of electrical voltage through the flow of an electrolyte over a charged surface may be used for energy transduction. Here, we show that enhanced electrical potential differences (i.e., streaming potential) may be obtained through the flow of salt water on liquid-filled surfaces that are infiltrated with a lower dielectric constant liquid, such as oil, to harness electrolyte slip and associated surface charge. A record-high figure of merit, in terms of the voltage generated per unit applied pressure, of 0.043 mV Pa^{-1} is obtained through the use of the liquid-filled surfaces. In comparison with air-filled surfaces, the figure of merit associated with the liquid-filled surface increases by a factor of 1.4. These results lay the basis for innovative surface charge engineering methodology for the study of electrokinetic phenomena at the microscale, with possible application in new electrical power sources.

3.2 Introduction

The motion of an aqueous electrolyte, such as salt water, over a surface may be harnessed for the generation of electrical voltage[32]. Indeed, the exploration of such electrokinetic phenomenon, and their possible use for energy conversion, have a long history, extending over the past two centuries (from Morrison & Osterle[33] and cited references). The relevant potential difference, termed as streaming potential (V_s), arises due to the relative motion of charged[34] species in the electrolyte, with respect to the fluid channel substrate with residual charges[31]. While superhydrophobic (SH) surfaces[6] have been posited to increase the ion velocity and the resultant potential difference, such enhancement has not been observed to date, due to the inability of the air in the SH surfaces to hold charge[35]. Here, we monitor the flow and measure the V_s of

higher dielectric constant (ε) NaCl based electrolyte (consisting of Na^+ and Cl^- dissolved in water) over a lower ε solid substrate/surface with an induced negative charge[2,36], in a microfluidic channel[37]. The electrically compensating positive counter-ions reside within the adjacent electrical double layer (EDL)[38], which consists of an inner layer with fixed counter-ions adsorbed onto the surface and a diffuse layer with mobile counter-ions, with a thickness of the order of the Debye length (λ_D). On application of a pressure difference (ΔP) across the two ends of the channel, say, through a mechanical pump: Figs. 3.1(a) - (c), the electrolyte flow would be mainly constituted from the mobile counter-ions in the diffuse layer, with the consequent charge separation yielding a streaming potential (V_s), proportional to the ε ($=\varepsilon_0\varepsilon_r$ – with $\varepsilon_0 = 8.854.\ 10^{-12}\ C^2\ N^{-1}\ m^{-2}$ as the free space permittivity, and ε_r as the relative permittivity of electrolyte *e.g.*, ~ 80 for 0.1 mM NaCl solution), the zeta potential (ζ) at the edge of the shear plane where the mobile ion motion occurs, and varying inversely with the dynamic viscosity of the electrolyte (η), and bulk electrolyte conductivity (κ), as described through the Helmholtz-Smoluchowski model[8,36]:

$$V_S = \frac{\epsilon\zeta}{\eta\kappa}\Delta P \tag{3.1}$$

The ζ is considered close to the substrate – electrolyte liquid interface, and is significant in that it determines the electrical potential that may be utilized[2,36] for the V_s. In the flowing electrolyte itself, there is a close to exponential decay of the surface potential over[38] λ_D. It should be noted that Eqn. 3.1 is based[39] on the assumptions of negligible surface (/substrate) conductivity and a very small EDL thickness[25], with Poiseuille flow of the electrolyte. Moreover, there is an implicit assumption of the *no-slip* boundary condition[40], where liquid adjacent to the substrate wall has a zero velocity with a finite flow velocity only at a certain distance (corresponding to the shear plane) into the fluid. Consequently, the ζ would be related to the electrical potential at the edge of the shear plane in electrokinetic flows over smooth surfaces[36,39]. Most work on harnessing the V_s through electrokinetic effects, to date, has been concerned with fluid flow over smooth surfaces (where the scale of roughness is smaller than λ_D), and consequently very small potential differences of the order of 18 mV may be predicted and obtained[8], in correspondence to Eqn. 3.1, *i.e.,* for 0.1 mM NaCl, with $\varepsilon_r \sim 80$, $\eta \sim 10^{-3}$ Pa · s, $\zeta \sim 25$ mV, $\kappa \sim 10^{-3}$ S m^{-1}, with $\Delta P \sim 1000$ Pa.

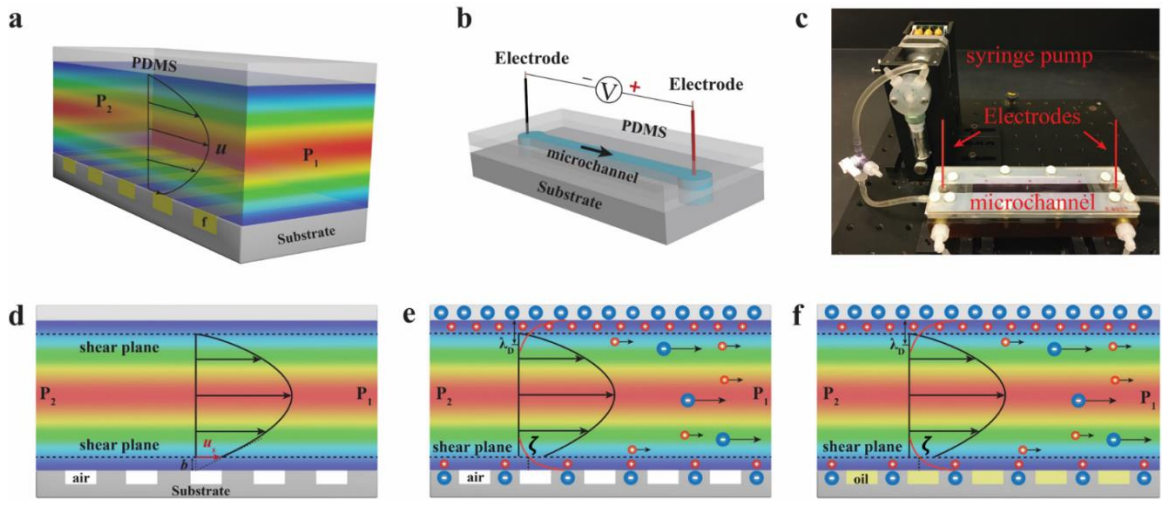

Figure 3.1 Electrokinetics over patterned and fluid filled surfaces. The phenomena were investigated (a) through monitoring the streaming potential (V_s) of salt water, under pressure driven flow, in a microchannel (of length 11.8 cm, width of 0.9 cm and height of ~250 μm). The upper surface of the channel was PDMS (poly-dimethyl siloxane) while the lower fluid-solid surface, was engineered with the fluid (*f*) such as oil or air. The velocity (u) profile with fluid slip, due to the pressure difference ($P_2 - P_1$) applied by syringe pump is indicated, (b) The schematic of the flow arrangement in the microchannel and its (c) experimental realization, wherein the top and the bottom surfaces were separated by a silicone rubber spacer to adjust the microchannel height, and Ag/AgCl electrodes were inserted in reservoirs at either end to measure the V_s. While (d) liquid flow over an *AFS* (air filled surface) yields a finite slip velocity (u_s), and slip length (b) the (e) flow of an electrolyte such as salt water yields a finite V_s due to surface charge (indicated as negative, here) induced influence on the electrolyte ions. (f) The V_s can be made significantly larger when the air is replaced by a water-immiscible liquid, such as oil yielding a liquid filled surface (*LFS*).

With the objective of obtaining significantly larger V_s, we indicate briefly the principles of our approach, which first involved the modulation of the effective ζ, through introducing fluid slip via groove patterned surfaces (air/liquid filled surface (*AFS/LFS*)) and modifying surface charges at the substrate surface. It has previously been considered, based on molecular dynamics based simulations[41], that slip may mobilize the Stern layer, significantly enhancing the ζ. The broad concept is that the shear plane/surface of shear (at which the electrolyte flow velocity is zero) is to be moved as close as possible to the substrate. As the surface electrical potential decays away from the substrate, the closer the shear plane is to the substrate boundary the larger the ζ with concomitantly increased V_s. Here, the zero velocity boundary condition at the surface ($y=0$) would be replaced with a Navier slip condition: $u_s\,(y=0) = b\,\frac{\partial u\,(y=0)}{\partial y}$) with b as the slip length[20,42], u_s as the slip velocity: Fig. 3.1(d). The larger the b, the greater the fluid velocity at

the surface by a factor of $(1 + \frac{b}{\lambda_D})$. A related apparent increase[43] in the ζ and the V_s may then be consequently obtained[44]. As much relatively large values of b of the order of 10 μm were thought to be obtained through the use of superhydrophobic (SH) surfaces[10], and given a λ_D of 9.6 nm with 1 mM NaCl, a b/λ_D of ~ 1000 is estimated, yielding large V_s. While non-uniform surface conduction[45], *e.g.*, as related to slip *to* no-slip transitions, may reduce such an enhancement a finite b would yet contribute to V_s, and may be aided by surface charge induced forces.

Our experiment results show that the V_s of NaCl electrolyte over *LFS* is increased by 1.4 times compared with that of electrolyte over *AFS*, which is due to the harness of both the slip and surface charge at liquid-liquid interface.

3.3 Methods

Design considerations and fabrication of air filled surfaces and liquid filled surfaces. The critical parameters in our channel surface design are (a) structural, *i.e.*, the interstitial fraction of *AFS/LFS*: ϕ - the ratio [= $d/(d + w)$], with an average ridge width (w) and spacing (d), as indicated in Fig. 3.2(a), (b) dimension, the channel length (L) and channel width (W) should be much larger than channel height (H), then the channel can be treated as two infinite parallel plates and the flow is Poiseuille flow, (c) pressure gradients, *i.e.*, over a range of 0-1000 Pa, with higher pressures yielding greater streaming potentials (V_s), and (d) the nature of the filling fluid, easier for oil with low surface tension to penetrate into the grooves. For instance, we have used in our electrokinetic flow experiments, ϕ ~ 0.5, 0.9 cm wide, 11.8 cm long and 250 μm high channel, with a pressure difference of ~ 1200 Pa, using GPL oil as a filling liquid, to generate maximal V_s.

The *LFS* were fabricated through filling oil into the grooves of a patterned surface, fabricated through photolithography and dry-etching. A Si wafer (n-type, <110>, thickness 500 μm) was cleaned with acetone and IPA, rinsed by DI water, and subsequently baked at 180 °C for 5 minutes. Negative photoresist

(NR9-3000) was coated on the Si wafer (3000 rpm for 40 s) and baked at 120 °C for 60 s. The pattern was defined through a mask (using the EVG 620) and developed (RD6) for 1 minute. Then the resist patterned wafer was subject to dry etching (using Oxford Plasmalab 100 RIE/ICP) to yield a trench depth (h) ~ 95 μm. The photoresist was then removed (using RR2 photoresist remover) over ~ 12 hours and any residues was further removed (using PVA TePla PS100 at 120 sccm, 200 W for 90 s). The grooved surface was coated with Parylene-C (using PDS 2010 Parylene Coater) to a thickness of ~600 nm.

For *LFS*, oils, *e.g.,* Dupont Krytox GPL 104, Castor oil, *etc.* was filled into the grooves of the patterned surface. The air-/liquid- patterned surfaces were imaged using environmental scanning electron microscopy (ESEM): FEI/Phillips XL ESEM and the FEI Quanta FEG 250 ESEM. We have indicated, *e.g.,* in Figure 3.2(c) that a lower ϕ - the ratio of the average groove width to the overall period, yields a larger V_s.

Choice of applied pressure and related flow rate. The electrolyte flow rate in the channel, constituted from rectangular plate geometry[46], was modulated through a syringe pump: Figure 3.1(c), and was transduced to an applied pressure (ΔP) based on the Poiseuille relation: $\Delta P = \frac{12\eta LQ}{wh^3}$ (Q is flow rate, L is channel length of ~ 11.8 cm, and h the channel height of ~ 250 μm). The ΔP over the channel length (where the other end was left open to atmosphere) motivated the pressure gradient driven flow, and for the experiment was in the range of 200 to1200 Pa, as measured through a manometer (UEI EM152 Dual Differential Input Manometer). It was observed that when the ΔP was larger (/smaller) than 1200 Pa (/200 Pa), that the generated streaming potential V_s was not stable.

Choice of liquid to fill the interstices in the liquid filled surfaces. For the fabrication of the *LFS*, the filling liquid (*e.g.,* Krytox® GPL 104 and castor oil) was chosen primarily on the basis of immiscibility with water/electrolyte. Additional criteria would be a low surface tension - for better penetration into the interstices, low viscosity and a smaller dielectric constant – to reduce electrolyte-oil interfacial shear stress.

We observe that the parylene coated Si surface was oleophilic (/hydrophobic), and that the chosen liquid or oil could penetrate the interstices easily: Figure 3.3(a).

3.4 Results

Voltage generation on air filled surfaces. To further understand the issues related to electrokinetics over surfaces with slip, we conducted experiments - see Figure. 3.1(b) and 1(c), where the electrolyte flow was driven in a microfluidic channel (of length: 11.8 cm, width: 0.9 cm and height: 250 μm) by a syringe pump with ΔP varied in the range of 0 - 1200 Pa to measure the V_s over ridged pattern surface morphology: termed as *AFS* (air filled surface): Fig. 3.1(e). The substrate material of *AFS* is silicon, coated by 600 nm hydrophobic parylene-C. The patterns were characterized through an interstitial/air fraction: ϕ_{air}, through the ratio [$= d/(d + w)$], with an average ridge width (w) and spacing (d): Fig. 3.2(a). We report results on samples with $\phi_{air} = 0.5$, $d = w = 18$ μm, for $\phi_{air} = 0.75$, $d = 27$ μm and $w = 9$ μm.

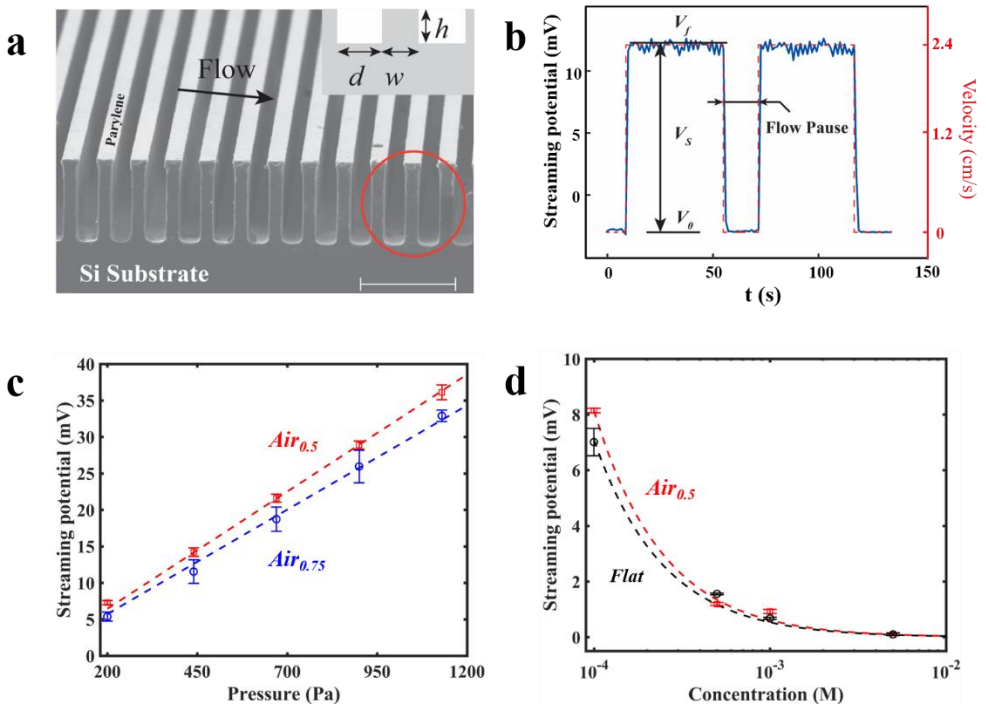

Figure 3.2 Streaming potential of air-filled surfaces. (a) A scanning electron microscope (SEM) micrograph of the grooved pattern surfaces with silicon as the substrate covered by parylene-C (thickness ≈ 600 nm), parameterized on the basis of the solid surface width (w = 18 μm), groove width (d = 18 μm), and pattern height ($h \approx 95$ μm), and the air fraction: ϕ_{air} [= d/ (d + w) = 0.5], and a solid fraction: ϕ_s= 1-ϕ_{air}. The flow direction is perpendicular to the grooves and indicated by the arrow. Scale bar is 100 μm. (b) The typical response of streaming potential (V_s) was measured, for a ϕ_s=0.5 *AFS*, through a syringe pump driven pressure, *e.g.*, with an applied pressure of 440 Pa, 0.1 mM L^{-1} NaCl here. The red dotted line indicated the average flow velocity in the channel. The measured voltage difference between a baseline value (V_o) and a final value (V_f) was considered as the V_s. (c) The measured V_s (0.1 mM NaCl solution) on an *AFS* (*i.e.*, $Air_{0.5}$, the subscript indicating the ϕ_{air}) scales linearly with the applied pressure (in the range of 200-1200 Pa), in accord with the Helmholtz-Smoluchowski model (Eqn. 3.1) with a lower value for V_s obtained for a smaller (/larger) ϕ_s (/ϕ_{air}) and rationalized as due to the absence of surface charges, and contributing zeta potential ζ, in the air regions. (d) The V_s scales with the salt water electrolyte conductivity and related concentration (I_c) through a log [I_c]/ [I_c] variation for both *AFS* ($Air_{0.5}$) and parylene coated flat surface (*Flat*) (concentration varying from 0.1mM L^{-1} to 5 mM L^{-1} at 200 Pa for (d)).

The consequent voltage-time trace: Fig. 3.2(b), was used to determine the V_s – monitored through a high resistance (>10 GΩ) voltmeter (Keithley 2700) connected across the Ag/AgCl electrodes placed at either ends of the channel: Fig. 3.1(c). However, a significant enhancement was not obtained for *AFS*, with an estimated[6] b of ~ 10 μm. It was interesting to note that a lower V_s was obtained for a larger ϕ_{air} (*i.e.*, smaller ϕ_s) for which a larger b would be expected: Fig. 3.2(c). Moreover, very little increase over a flat unpatterned surface was obtained comparing $Air_{0.5}$ and *Flat*: Fig. 3.2(d). The lower V_s of *AFS* may be

rationalized as due to the absence of a surface charge in the air regions[25], which overwhelms the contribution of the slip.

While the data here seems to indicate the general validity of Eqn. 3.1, in terms of a linear V_s - ΔP plot, the slope of the obtained experimental curves would then be directly connected to the ε, ζ, η, and the κ. Such parameters are then intimately connected, *i.e.*, while independent variation would be difficult to discern experimentally, theoretical or computational input (which is outside the purview of the present experimental work) may be able to yield guidance for explicit dependence. The net V_s has been construed to be related to a weighted summation of ζ in the no-slip region (over the solid fraction of the surface, *i.e.*, ζ_{NS}) and the slip region (*i.e.*, over the air of the *AFS, i.e.*, ζ_S) [35]. The very small ζ_S would adversely affect the V_s and as seen through our experiments, overwhelms the slip length related contribution. Related correspondence of the obtained V_s to the ζ as well as the electrolyte conductivity, which is proportional to I_c (the counter-ion concentration) was determined through a log [I_c]/ [I_c] dependence: Fig. 3.2(d).

Increased voltage on liquid filled surfaces. Subsequently, we deployed patterned surfaces where the air pockets were infiltrated by a water immiscible liquid, *e.g.*, oil, of a higher density compared to the NaCl electrolyte: Fig. 3.3(a). Such liquid filled surfaces (*LFS*) were hypothesized to yield a finite ζ_S at the oil interfaces, in addition to a non-zero *b*. The *LFS* were fabricated through replacing the air in groove patterned arrays by water-immiscible liquid, such as oil, and may be designed to exhibit various degrees of fluid slip[27,47,48], as well as electrical voltages,– significantly larger than on air-filled or SH surfaces. The oil filling was found to be reliable and stable.

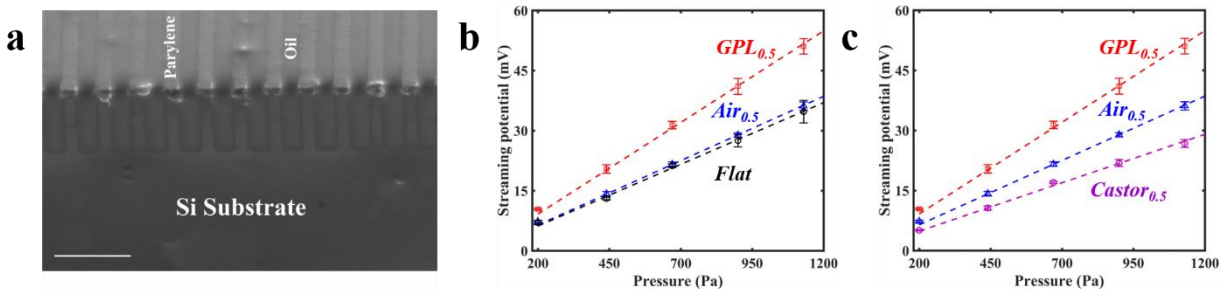

Figure 3.3 Enhanced streaming potential at liquid filled surfaces. Enhanced streaming potential (V_s) was obtained by (a) filling the grooves with salt water immiscible oil, *e.g.*, Krytox GPL 104, (scale bar is 100 μm) (b) a significantly larger V_s was obtained for an GPL 104 oil filled surface (*i.e.*, $GPL_{0.5}$, with the subscript now indicating the interstitial fraction of oil), compared to one with air ($Air_{0.5}$) and even compared to a *Flat* solid substrate (all measured using 0.1 mM L^{-1} NaCl solution with applied pressure as 1200 Pa). (c) The V_s could be larger or smaller compared to the control *AFS*, depending on the choice of the liquid in the *LFS*, *e.g.*, GPL oil and castor oil ($Castor_{0.5}$), respectively.

Additionally, the use of oil with a lower ε_r compared to the flowing electrolyte would mean that the electric field from the wall is effectively propagated. Through the use of Krytox GPL 104 oil ($\varepsilon_r \sim 2.1$, $\eta \sim 340$ cP), a significant enhancement of the V_s by 50%, to around ~ 52 mV, compared to that of $Air_{0.5}$ was observed: Fig. 3.3(b), attesting to the utility of the *LFS*. However, it was noted that the obtained V_s critically depends on the choice of the oil in the *LFS*. Broadly, a larger ε_{oil} seems to yield a lower V_s. For instance, a factor of two smaller value was obtained for a castor oil ($\varepsilon_r \sim 4.7$, $\eta \sim 312$ cP) filled *LFS*: Fig. 3.3(c). The enhanced van der Waals energy of interaction[1] between the oil and the electrolyte, proportional to the dielectric constants, and the related mutual electric polarizabilities causes a larger friction. The consequent movement of the shear plane away from the solid substrate would result in a lower zeta potential and V_s.

The electrolyte flow over the *LFS* as well as the adjacent solid surface was parameterized[46] through the use of a material dependent surface charge density (σ) related to $\zeta = \frac{\lambda_D \sigma}{\epsilon}$ and fluid slip at the respective interfaces. From literatures, for the top surface of the channel (constituted from poly-dimethyl siloxane: PDMS), σ_{PDMS}[49] ~ 18 mC m^{-2}, while for the bottom patterned surfaces, we use σ_{oil}[50] ~ 1.8 mC m^{-2} and σ_{parylene}[51] ~ 3.6 mC m^{-2}. The σ and the velocity slip is inhomogeneous along the length of the channel, but constant along the channel width. The no-slip hydrodynamic boundary condition was assumed to hold true at all solid-electrolyte interfaces, while a Navier slip boundary condition over the flowing electrolyte-oil

interface was assumed, with a finite slip velocity: u_s and slip length: b. For a hydrophobic surface, the b may be approximated[6] to be of the order of d, *i.e.*, ~ 18 μm. A correspondence to a Cassie state-like channel flow (with no electrolyte penetration into the grooves of the patterned surface) for *LFS* surface may be seen. It should be noted that simulations considering the continuity of tangential shear stress across the electrolyte-oil interface also obtained the V_s very close (within 1 %) to the results obtained through an assumption of a slip length.

Modeling of electrolyte flow over the liquid filled surfaces. We partition[39] the pressure gradient driven electrolyte flow, following experiment, over the *LFS* as the superposition of (i) hydrodynamic flow, with fluid slip over electrically neutral surfaces, and (ii) an electrokinetic flow, with no-slip fluid flow over flat electrically charged surfaces: Figs. 3.4(a) – (c). A multiphysics model coupling the Nernst-Planck-Poisson (N-P-P) equation with the Stokes Equation, was deployed to determine the volumetric charge density profiles. The velocity profile combined with the simulated volumetric charge density profile along the channel, as indicated in Fig. 3.4(d), arises due to the difference of ionic concentrations between the counter-ions and co-ions. The resultant horizontal electric field, is responsible for the observed streaming potential (V_s). The calculated average electrolyte velocity of 6 cm s^{-1} is in agreement with that expected from Poiseuille flow along the channel, with the estimated u_s at the oil-electrolyte interface of ~ 2 cm s^{-1} at ΔP ~ 1200 Pa. Additionally, and given the relatively large groove widths, the influence of the surface conductivity on the obtained results would be relatively small[44].

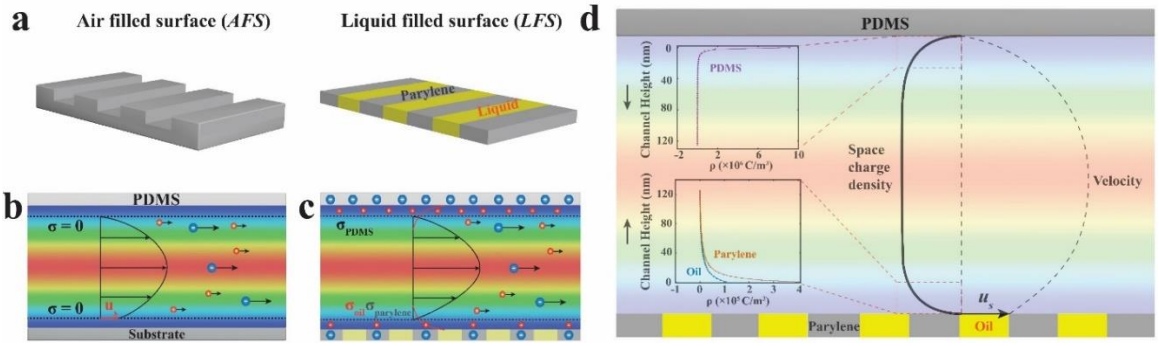

Figure 3.4 Parametrization and modeling of charged fluid-solid surfaces. (a) The surface charge density (σ) of an *AFS* (air filled surfaces) varies between zero (at the air) and a finite value at the solid, while a nominally planar *LFS* (liquid filled surfaces) maintains a larger value of the σ. The electrokinetics on the *LFS* was considered in terms of a superposition of (b) hydrodynamic flow, with fluid slip over electrically neutral surfaces and (c) an electrokinetic flow, with no-slip fluid flow over electrically charged surfaces, and solving the coupled Nernst-Planck-Poisson (NPP) equation along with the Stokes Equation, to determine the (d) velocity profile as well as the volumetric charge density (ρ) profiles. The insets indicate the computed variation of the ρ at the top PDMS surface and the bottom *LFS*.

3.5 Discussion

Excellent agreement of the simulations with experimentally observed values of the streaming potential was observed through considering a reduced $\varepsilon_r \sim 28$, over a distance of $\sim 3\lambda_D$ proximate to the *LFS* and an $\varepsilon_r \sim 78$ beyond - correspondent to the bulk solution. Such aspect is in accord with the use of different values of the dielectric constant for the inner and outer regions of a solid -solution interface[39]. The *LFS*, consisting of both oil as well as solid surfaces, may yield an uneven shear plane with fascinating implications for novel electrokinetic phenomena[52,53], such as localized concentration polarization[44], *etc.* Our work also indicates that a heterogeneous surface could be patterned through the use of discrete surface charge density or applied potentials, mimicking a superhydrophobic surface, and making a connection with electro-wetting applications, as well as with significant literature on the modeling and parameterization of liquid flows on striped surfaces exhibiting alternate regions of slip and no-slip, with[54,55] and without[30] surface charge.

A more detailed investigation of several issues related to the interplay of enhanced surface charge as well as increased slip velocity at the flowing electrolyte - *LFS* interface would then be warranted. It has

been indicated, for instance, that an increased V_s would result due to the larger ion convection currents[56]. Additionally, viscous effects may be playing a major role[57,58]. As the coefficient in Eqn. (3.1), intimately connects the ε_r, and the η, a decrease in the former may not be readily deconvoluted from an increase in the latter experimentally. In our numerical simulations, an increase in the η by a factor of ~ 2.5 over the equivalent length scale (from a bulk value of 0.89 cP to 2.19 cP) was necessary to obtain the experimentally observed streaming potentials, assuming that the ε_r is ~ 78.

Our experiments have deep scientific implications underlying fluid flow interfacing with both air and liquid as well as fluid shear at a surface, and electrokinetic phenomena as related to the localized variation of the zeta potential and nonlinearity. We anticipate that our work would revitalize research related to the fabrication of alternate electrical voltage/power sources from liquid flow over charged surfaces. Other anticipated applications extend to electrophoretic applications in biological separations (cell transport, manipulation[59], and interactions[60]), as well as voltage sources for lab-on-a-chip applications[61].

3.6 Conclusion

In summary, our work has experimentally demonstrated the largest figure of merit thus far[62–65] to the best of our knowledge, with primary focus on methodologies related to enhance the streaming potential (V_s) per unit pressure difference (ΔP), through the use of liquid filled surfaces (also see Supplementary Note 6 for considerations related to overall electrokinetic efficiency). The use of the *LFS* yields a factor of 1.4 larger figure of merit compared to that obtained through the use of the *AFS*. It has been shown that larger voltages, through a measured streaming potential, may be achieved through careful engineering of the coupled electric field and fluid flow. The application of the related increase in the electrokinetic energy conversion efficiency would need further optimization of the fluidic and electrical impedances, in concert with the streaming conductance, as matched to an appropriate load[66]. Concomitantly, unipolar transport (where for example, either Na^+ or Cl^- ions are transported[67]) through electrical double layer overlap[46,68] in

nanoscale channels, may be coupled with *LFS* to yield much larger voltages, comparable to that of batteries[69].

3.7 Acknowledgement

This chapter, in full, is a reprint of the materials as it appears in Fan, B., Bhattacharya, A. and Bandaru, P.R., Enhanced voltage generation through electrolyte flow on liquid-filled surfaces, Nature Communications, 9, 4050, 2018. The dissertation author was the primary investigator and author of this paper. The authors are grateful for support from the National Science Foundation (NSF: CMMI 1246800 and CBET 1606192). We also appreciate the assistance of Prof. J. Friend and P. Chen for help with imaging and Dr. S. Rubin for discussions.

3.8 Supplementary materials

3.8.1 Geometrical parameters for the construction of air filled surfaces (*AFS)* and liquid filled surfaces (*LFS*):

For the influence of surface geometry alone, we compare the results of *Flat* (unpatterned surface), and the air-filled surfaces (*AFS*): $Air_{0.5}$ and $Air_{0.75}$, as indicated in Figures 3.2(c) and (d). The air in the *AFS* can reduce the friction between the flowing liquid electrolyte and patterned surface which helps in the increase of the streaming potential (V_s). However, a non-charged liquid-air interface will have no contribution to streaming potential[34,35]. Consequently, the V_s of $Air_{0.5}$ is only a little larger than compared to the *Flat* case and the V_s of $Air_{0.75}$ is even smaller, presumably due to an increase of non-charged liquid-air areas.

The aspect of nano- and micro-scale roughness was considered and found to be of much less importance compared to the groove width. The nominal roughness of the parylene coated surface was found

to be R_a = 1.25 nm $\pm$ 0.19 nm (as determined through Dektak 150 Surface Profilometer) and the obtained streaming potential was insensitive to variations around such values. Generally, a roughness of < 6 nm has minimal effects on the slip length and flow rate[70], and can be considered hydrodynamically smooth[71].

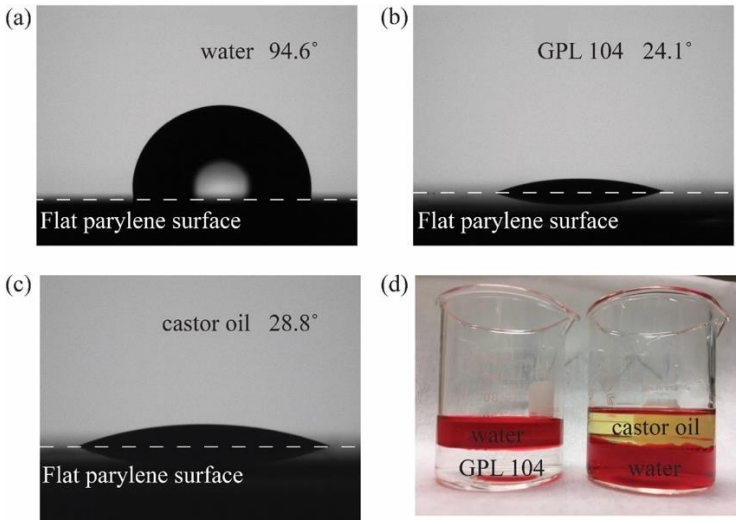

Supplementary Figure 1 The contact angle of (a) water, (b) GPL 104, and (c) castor oil on parylene coated flat Silicon surface were measured using Ramé-Hart Model 190 Contact Angle Goniometer. The measured results are 94.6°, 24.1°, 28.8° for water, GPL 104 and castor oil, respectively. It is then clear that parylene is hydrophobic (/oleophilic). (d) shows that the GPL 104 oil as well as the castor oil is immiscible with water.

Supplementary Table 1 | Physical properties of filled fluids (*data from* DuPont® Performance Lubricants, 2015**)**

Oils	**Density (g/cm^3)**	**Kinematic Viscosity (cm^2/s)**	**Dynamic Viscosity (mPa·s)**	**Dielectric Constant**	**Surface Tension (mN/m)**
Krytox® 104	1.93	1.77	340	2.1	18
Molivera Organics Castor Oil	0.96	3.25	312	4.7	39

3.8.2 The pressure dependence of V_s and the numerical estimation of the surface potential (ζ)

In the chosen pressure range, that the V_s was linearly proportional to the applied ΔP, following the Helmholtz-Smoluchowski relation: $V_S = \frac{\epsilon\zeta}{\eta\kappa}\Delta P$, as shown in Figures 3.2(c), 3.3(b), and 3.3(c). From the slope of the V_s - ΔP curve, we estimate the surface potential (ζ) at the edge of the shear plane, assuming an the electrolyte permittivity: $\varepsilon (= \varepsilon_o\varepsilon_r)$ with ε_r as the relative permittivity, *e.g.,* ~ 80 for 0.1 mM NaCl solution), η*:* the dynamic viscosity of the electrolyte (~ 10^{-3} Pa·s), and a bulk electrolyte conductivity ($\kappa \sim 10^{-3}$ S/m), which are listed in Supplementary Table 2, below.

Supplementary Table 2 | Linear fitting results and ζ

Sample	R^2	Slope (mV/Pa)	ζ (mV)
Flat	0.9972	0.03081	44.2
$Air_{0.5}$	0.9997	0.03117	46.1
$Air_{0.75}$	0.9963	0.0286	41.0
$GPL_{0.5}$	0.9996	0.04392	65.6
$Castor_{0.5}$	0.9963	0.02418	34.7

3.8.3 Estimates of the overall slip length (b_{eff}) from averaged surface potential (ζ)

The ζ values listed in Supplementary Table 2, may be considered an averaged/effective value($= \zeta_{eff}$) considering the top (*PDMS*) and bottom (the *LFS*, constituted from the *parylene* and the *oil* in the *interstices*) surfaces of the channel. Based on the effective medium approach (EMA)[35], we consider a weighted summation of the ζ_{PDMS}, $\zeta_{parylene}$, and $\zeta_{interstice}$ as follows:

$$\zeta_{eff} = 0.5\zeta_{PDMS} + 0.5\zeta_{parylene} \quad \text{(S3-1)}$$

$$\zeta_{eff} = 0.5\zeta_{PDMS} + \frac{b_{eff}}{\lambda_D}(0.25\zeta_{parylene} + 0.25\zeta_{interstice}) \quad \text{(S3-2)}$$

The reported $\zeta_{parylene}$ is 17.5 mV at 10 mM NaCl solution[72], consequently $\zeta_{parylene}$ was estimated to be ~ 35 mV for the 0.1 mM electrolyte used in our studies, based on the relation[36] $\zeta \sim \log[I]$. The ζ_{PDMS} was estimated to be ~ 53.4 mV based on the first equation using $\zeta_{eff} = 44.2$ mV for *Flat*. Such

an estimate for the ζ_{PDMS} seems to be in reasonable accord with literature, considering that there may be many affecting factors[36,73], *e.g.,* counter-ion type, pH of the solution and temperature. The $\zeta_{interstice} = 0$ mV for air[35]. Then, the b_{eff} for $Air_{0.5}$ can be estimated as 66.5 nm based on the second equation. Given that[74] the ζ_{oil} is ~ 69 mV, the effective slip length b_{eff} for the $GPL_{0.5}$: would be ~ 44.9 nm. The b_{eff} can also be estimated for $Air_{0.25}$ and $Castor_{0.5}$ using the same method and all the results are listed in Supplementary Table 3.

Supplementary Table 3 | Estimates of the *effective* slip length: b_{eff}

Sample	b_{eff}(nm)
$Air_{0.5}$	66.5
$Air_{0.25}$	98.0
$GPL_{0.5}$	44.9
$Castor_{0.5}$	9.2

The b_{eff} of $Air_{0.75}$ is larger compared to that of $Air_{0.5}$ and maybe related to the larger amount of air, in the former. The b_{eff} of *GPL oil* is smaller due to a larger viscosity, compared to air, while the b_{eff} of *castor oil* is even smaller due to a larger dielectric constant.

While significant care was taken in removing the oil from the surface in the use of the *LFS*, there is a possibility that the oil may partially cover the parylene surface. Consequently, the effective medium approach (EMA) aspect may indeed be considered an approximation. Previously, we used $\phi_{parylene}$ = 0.25 and $\phi_{interstice}$ = 0.25 (assuming that parylene area was not covered by oil) and obtained an effective slip length (b_{eff}) of ~ 44.9 nm for $GPL_{0.5}$. However, even with $\phi_{parylene}$ = 0.1 and $\phi_{interstice}$ = 0.4 (assuming that 80% of the LFS was covered by oil), the b_{eff} is ~ 37.5 nm, a change of ~ 16%. Consequently, the use of the EMA seems to be a reasonable approximation.

3.8.4 Pressure-driven electrokinetic flow with *no* hydrodynamic slip

To describe electrolyte flow, we modeled through self-consistent finite element simulations (COMSOL®), the local fluid velocity at a point ($\boldsymbol{u}$), the respective ionic species concentration (c_i), and electric potential (ϕ). The relevant mass conservation equations, and the Stokes equation were coupled with the Nernst-Planck-Poisson (*N-P-P*) models, as described below.

Let i= 1, 2 represent the ionic species present in the electrolyte, *e.g., i*=1 refers to Na^+, while *i*=2, refers to the Cl^- species. The flux conservation equation[75] of each ionic species, i, is

$$\frac{\partial n_i}{\partial t} = \nabla \cdot \boldsymbol{J_i} \tag{S4-1}$$

where $\boldsymbol{J_i}$ is the ionic flux vector and n_i is the number density of ions per unit volume. $n_i = c_i * N_{Av}$ where c_i is the concentration of each ionic species in moles/L (M) and N_{Av} is the Avogadro constant = 6.02 x10^{23} /mole. For steady state flow: $\nabla \cdot \boldsymbol{J_i} = 0$.

The Nernst-Planck (*N-P*) equation[32,39,76]: Eqn. (S4-2) below, considers the motion of ions in a fluid as a function of fluxes due to convection, diffusion, as well as ion migration under the effects of electrostatic forces.

$$\boldsymbol{J_i} = n_i \boldsymbol{u} - D_i \nabla n_i - \frac{z_i e\, n_i D_i}{k_B T} \nabla \phi \tag{S4-2}$$

D_i is the respective species diffusivity, *i.e.,* D_{Na^+} = 1.13 x 10^{-9} m^2 /s and $D_{Cl^-} = 1.0$ x 10^{-9} m^2 /s. z_i is the valence of each ionic species. $z_{Na^+} = 1$ and $z_{Cl^-} = -1$, k_B is the Boltzmann constant = 1.38 x 10^{-23} J/K and T = 298 K. The $\boldsymbol{u}$ is obtained through the Stokes' equation[40]: Eqn. (S4-3),

$$-\nabla p + \mu \nabla^2 \boldsymbol{u} + \rho_f \nabla \phi = 0 \tag{S4-3}$$

Here, pressure gradient driving the flow (∇p), the viscous force ($\mu \nabla^2 u$, with μ as the dynamic viscosity) and the electrical body force (=$\rho_f \nabla \phi$), with ρ_f as the volumetric space charge density in the electrolyte due to the presence of free charges, *e.g.,* counter-ions near the surface, are all considered. The electric potential (ϕ) is obtained from the Poisson (*P*) equation[77]:

$$\nabla \cdot (\epsilon_0 \epsilon_r \nabla \phi) = \rho_f \quad \text{(S4-4)}$$

ϵ_0 is = $8.854 \cdot 10^{-12}$ C^2/Nm^2- the permittivity of free space and $\epsilon_r$is the relative permittivity of the species near the wall. The ϕ from Eqn. (S4-4) and the n_i from Eqn. (S4-2) are coupled through:

$$\rho_f = \sum_{i=1}^{2} z_i e \, n_i \quad \text{(S4-5)}$$

Eqns. (S4-2), (S4-3), (S4-4), and (S4-5) are solved self-consistently, and used to obtain (i) $\boldsymbol{u}$, and (ii) ϕ and related n_i, at any point (*x,y*) in the channel. Here, *x* is along the direction of fluid flow along the length of the channel, and *y* is the vertical coordinate – along the height of the channel. The $\boldsymbol{u}$ yields the local velocity, and is averaged along the width of the channel for the average velocity. The $V_{s,j}$ developed between any two points (x_j, y_j) and (x_{j+1}, y_j) along the channel is then computed from $|\phi(x_j, y_j) - \phi(x_{j+1}, y_j)|$. The net V_s was aggregated from such individual contributions along the length of the channel. The mesh size, for the finite element simulations, was chosen to be 5 nm at both the top and bottom walls outwards.

Boundary Conditions: For the N-P equation (Eqn. S4-2), the bulk concentration $\boldsymbol{c_o} (= \boldsymbol{c_{Na^+}} = \boldsymbol{c_{Cl^-}})$ = 0.1 mM, was kept constant for both the electrolyte ion species at both inlet and outlet, as well as at the centerline of the channel, assumed to be far outside the electrical double layer (EDL), as the Debye length ($\boldsymbol{\lambda_D} = \sqrt{\frac{\epsilon_o \epsilon_r k_B T}{e^2 c_i}}$) was estimated to be ~ 30 nm. The difference of ionic concentration between counter-ions and co-ions, yields a net charge profile density along the height of the channel. The flux normal to top and bottom walls $\boldsymbol{J_i} = \boldsymbol{0}$.

For the Poisson equation (Eqn. S4-4), the surface charge density (σ) at the top wall[49]: σ_{PDMS} = -18 mC/m^2, while at the bottom surface, (i) at the oil[74]-electrolyte interface is σ_{oil}= -1.8 mC/m^2, and (ii) for the parylene[51]-electrolyte interface is $\sigma_{Parylene}$ = - 3.7 mC/m^2. The σ values are related to the surface electrical field. The outlet was set at zero potential (/ground). It was assumed that the electric field due to EDL and that due to generated streaming potential were completely decoupled. The ϕ at the center-line of flow, in the middle of the channel, *i.e.,* $\phi\ (y = H/2) = 0$ and far away from the EDL at the surface was set to zero.

For the Stokes equation (Eqn. S4-3), the inlet pressure was set to 1200 Pa, while the outlet was set to zero. The no-slip hydrodynamic boundary condition was assumed to hold true at all interfaces.

3.8.5 Hydrodynamic flow with no surface charge but slip at the oil-electrolyte interface

Here, the Stokes Equation (without any electrical body force) is the governing equation

$$-\nabla p + \mu \nabla^2 u = 0 \tag{S5-1}$$

The inlet pressure was set to 1200 Pa, while the outlet was set to zero. A Navier slip boundary condition: $u_s\ (y=0) = b\frac{\partial u\ (y=0)}{\partial y}$ over the flowing electrolyte-oil interface was assumed, with a finite slip velocity: u_s and slip length: b). For a hydrophobic surface the b may be approximated[29,78] to be at least *d, i.e.,* ~ 18 μm.

3.8.6 Considerations related to the figure of merit (in mV/Pa) and energy conversion efficiency

Our focus, in the presented work, was less on the energy conversion efficiency and *more* on methodologies to enhance the streaming potential (V_s) per unit pressure difference (ΔP), *i.e.,* $\left(\frac{V_s}{\Delta P}\right)$. Indeed, our work has experimentally demonstrated the *largest figure of merit*, thus far, in terms of the voltage generated per unit applied pressure, in comparison to previous experimental work[79–82].

More specifically, the fluid flow to electrical conversion efficiency (*Eff.*) = P_{out} /P_{in}, where the output power: P_{out} ($=\frac{1}{4}V_s \cdot I_s$), I_s ($= V_S\frac{A\sigma}{L}$) is the streaming current, with A ($= w \cdot h$) as the cross-sectional area of the channel of width: w, and height: h, and $P_{in} = Q \cdot \Delta P$, Q is the flow rate ($=\frac{Gh^3}{12\eta}$), with G as a constant pressure gradient, and η the viscosity.

Then, the *Eff.*$= \frac{3V_S^2\sigma\eta w}{\Delta P L G h^3} = 3\left(\frac{V_s}{\Delta P}\right)\left(\frac{V_s}{L}\right)\left(\frac{\eta\sigma}{G}\right)\left(\frac{w}{h^2}\right)$. For a given electrolyte concentration (fixed σ) and flow velocity (a given u), <u>both</u> $\left(\frac{V_s}{\Delta P}\right)$ and $\left(\frac{w}{h^2}\right)$are important. While the former, *i.e.,* $\left(\frac{V_s}{\Delta P}\right)$ was considered in detail in our work, the geometrical factor: $\left(\frac{w}{h^2}\right)$ may be significantly enhanced through the use of

nanoscale diameter channels (small *h*) with the overlap of double layers, as seen for example, in the work by van der Heyden, *et al, Nanoletters,* vol. 6, p. 2232, (2006). We used channels of the order of 250 μm in height over which most of the electric field is zero and a finite field is obtained only close to the channel surfaces of the order of 0.1 μm (the Debye length). Consequently, the estimated energy conversion efficiencies in our work is quite small of the order 10^{-3} %, employing the computational methodology indicated in van der Heyden, *et al, Nanoletters,* vol. 6, p. 2232, (2006). More specifically, the efficiency values are ~ $7.7 \cdot 10^{-4}$ % (through the use of the oil in a *LFS*), ~ $3.8 \cdot 10^{-4}$ % (on an *AFS*), and ~ $3.5 \cdot 10^{-4}$ % (on a flat unpatterned substrate).

An important point to note is that the energy conversion efficiency may be improved by more than a factor of two through the use of LFS compared to the flat/AFS substrates. We may expect that the efficiency of nanochannels may be further enhanced by using *LFS*, and will be one of the focus areas of future work.

Chapter 4 Modulation of streaming potential and slip characteristics in electrolyte flow over liquid-filled surface

4.1 Abstract

A significant enhancement in the streaming potential (V_s) was obtained in experiments considering the flow of electrolyte over liquid filled surfaces (*LFS*), where the grooves in patterned substrates are filled with electrolyte immiscible oils. Such *LFS* yield larger V_s (by a factor of 1.5) compared to superhydrophobic surfaces, with air-filled groves, and offer tunability of electrokinetic flow. It is shown that the density and viscosity, surface tension as well as the dielectric constant of the filling oil, in the *LFS,* determines V_s. Relating a hydrodynamic slip length to the obtained V_s offers insight into flow characteristics, as modulated by the liquid interfaces in the *LFS.*

4.2 Introduction

Electrokinetic flows, considering the movement of electrolyte relative to another charged surface, are important for understanding the effects of charge accumulation and dispersion, with applications ranging from power generation[83–85] to biochemical separations[31,86]. For instance, in pressure driven flows, the flow of excess ions in the electrical double layer (EDL) near the surface, would generate a streaming current, and in the absence of such current – an ion accumulation related streaming potential (V_s). The exploration of the use of this phenomenon for energy sources has a long history[87,88], and has also received much attention recently, from a micro- and nano-fluidics pesrpective[46,83,89]. For example, the overlap of the EDLs in nanoscale channels could lead to unipolar flows mimicking battery-like behavior. However, considering that flow and throughput restrictions are a major constraint at the nanoscale[90], we focus our work as presented here on engineered microscale channels for obtaining high V_s.

Fluid flows over smooth surfaces with no-slip conditions, yield low streaming currents and potential. It has then been indicated that enhanced electroosmotic mobility: M, may be obtained through the use of patterned[91,92] or superhydrophobic (SH) surfaces[5], in both laminar and turbulent flows. The basis is that the aiding of the counter-ion motion near the surface would enhance the electroosmotic current and the related V_s. From the Helmholtz-Smoluchowski relation[32], $M = \frac{\varepsilon\zeta}{\eta}$, where ε ($= \varepsilon_o\varepsilon_r$, with ε_o=8.854·10^{-12} C^2/Nm^2 is the vacuum permittivity and ε_r is the relative permittivity) is the dielectric constant of the electrolyte, ζ is the zeta potential, and η is the viscosity. However, such an increased mobility is based on the requirement that the no-shear/slipping surfaces have a significant charge density, and of a similar magnitude and sign as that of the no-slip surface in fluidic channels.

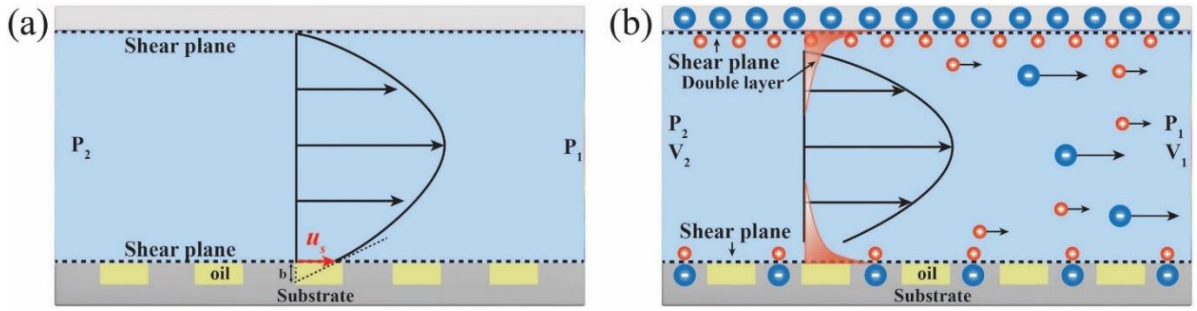

Figure 4.1 Large (a) slip velocities (u_s), as well as (b) electrokinetic streaming potentials ($V_s = V_1 – V_2$) may be generated through Poiseuille type electrolyte flow (under a pressure difference $\Delta P = P_1 - P_2$) over a liquid filled surface (*LFS*), with interstices/grooves filled with liquids of varying physical parameters, such as the density, dielectric constant, viscosity, *etc.* The positive and negative charges are indicated by the red and the blue circles. A larger V_s may be generated due to a larger ζ (the zeta potential).

Traditionally, SH surfaces were fabricated through the use of air to promote slip, *e.g.*, in patterned[29,93] or non-smooth surfaces[7,9,10], with a flat air-electrolyte interface. Through much insight, it was determined that only a charged liquid-air interface could enhance the streaming potential[94–96]. It was found, for instance, that the V_s for flow over uncharged liquid-air interface was similar to that of the homogeneously charged smooth surface for low EDL thicknesses and ζ [94,95], and may be smaller compared to that obtained from a smooth surface with high zeta ζ [96]. There is also considerable ambiguity on the

electrical character of the air-electrolyte interface, as to whether there is a charge at all *to* yielding an electrical potential due to residual OH^- ions.

We circumvent such ambiguity in our work using liquid (of an appropriate ε_r) filled into the interstices of patterned surfaces, fabricated to mimic SH character. Consequently, a definitive charge density would be ensured at the flowing electrolyte slipping surface[97], promoting the conditions for obtaining large streaming potentials: Fig. 4.1. The shear plane is generally understood as the location at which the fluid starts to move and would be expected to be located at the liquid-liquid interface and the solid-liquid interface. Fig. 4.1(a) emphasizes the flow profile (incorporating the slip velocity: u_s, as well as the associated slip length: b) over a liquid filled surface (*LFS*) [98], while Fig. 4.1(b) depicts the associated electrokinetic flows over the *LFS.* In this study, we investigate the characteristics of the *LFS*, which may be used for enhancing the magnitude of the associated V_s. We also show that the use of such surfaces enables a simultaneous decrease of the fluid drag[99–102], and increased flow[103,104] coupled with an increase in the V_s.

4.3 Experiment section

Fabrication and characterization of hybrid surfaces: the *AFS* and the *LFS*. A reference air filled surface (*AFS*) – consisting of rectangular ridges and troughs, was fabricated through photolithography processes and is shown in Fig. 4.2(a). Briefly, a Si wafer (n-type, <110>, thickness 500μm, from University Wafer) was cleaned with acetone, IPA, and rinsed by DI water, then baked at 180° C for 5 minutes. Negative photoresist NR9-3000 was coated on Si wafer at 3000 rpm for 40 s and then baked at 120° C for 60 s. The specific pattern was defined through a mask aligner (EVG 620) and developed (using RD6) for 1 minute. Subsequently, the resist patterned wafer was subject to dry etching (using Oxford Plasmalab 100 RIE/ICP) to yield a trench depth (h) ~ 95μm. The etched Si wafer was then put in RR2 photoresist remover over ~ 12 hours and any resist residues further removed (using PVA TePla PS100 at 120 sccm, 200 W for 90 s). Finally, the grooved surface was coated with Parylene-C (using PDS 2010 Parylene Coater) to a thickness

of ~ 600 nm. The basis *AFS* was defined through an air fraction, $\phi_a = \frac{d}{d+w}$ - the ratio of the trough width (d) over one period length ($d + w$). The surfaces were imaged using environmental scanning electron microscopy (ESEM): FEI/Phillips XL ESEM and the FEI Quanta FEG 250 ESEM, respectively: Fig. 4.2(b): *AFS*, and Fig. 4.2(c): *LFS*.

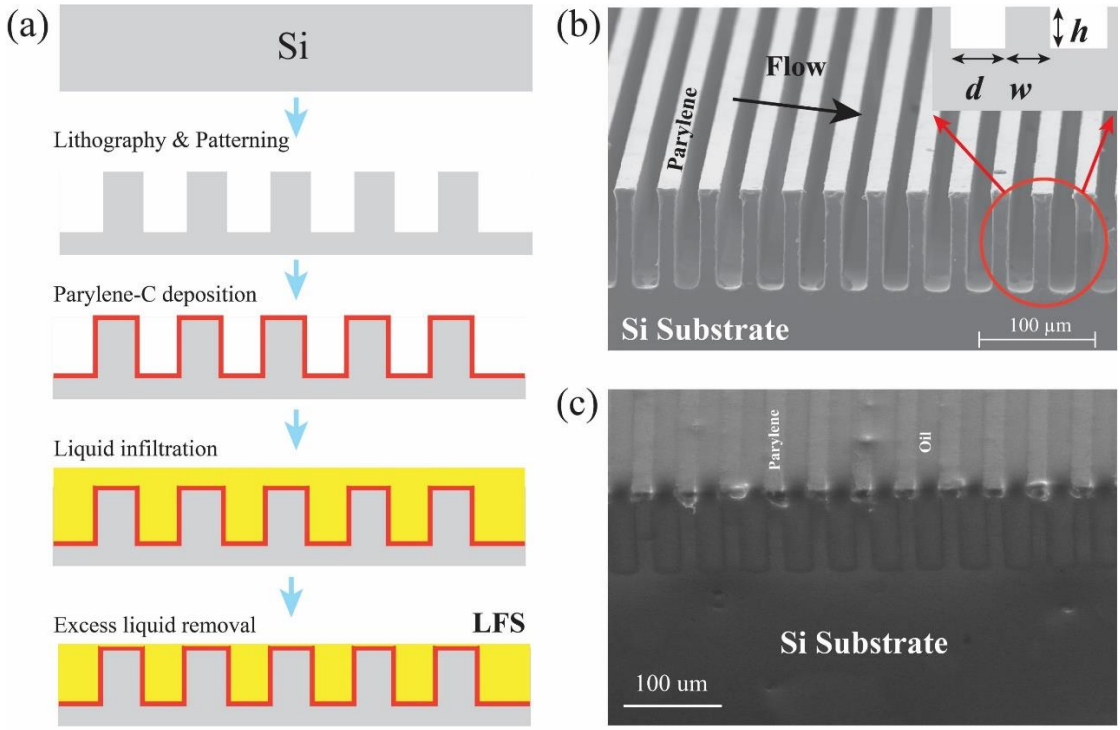

Figure 4.2 A liquid filled surface (*LFS*) was fabricated through (a) lithographic procedures to synthesize a surface with ridges and grooves, and subsequent deposition of a uniform parylene film. The grooves are filled with a liquid (immiscible with the electrolyte and with low surface tension) and subsequently the *LFS* is planarized. (b) The surface, as indicated through a scanning electron microscope (SEM) image is defined through the width of the trough (d) and ridge (w), as well as the height (h). (c) An image of a practical *LFS*, indicating grooves filled with oil.

Due to the oleophilicity of the *AFS*[105], oils immiscible with water and with low surface tension, *e.g.*, Dupont Krytox GPL 104 (General Purpose Lubricant) - a fluorinated synthetic oil, castor oil, and synthetic motor oils (0W-20 and 20W-50), can be filled into the troughs of the patterned surface to yield a *LFS*, located at the bottom of the micro-fluidic channel. The physical parameters for the oils used in the *LFS* are listed in Table I. The oil was spread evenly on the surface via soft brush and any excess oil was removed

from the top of the *LFS*. Detailed microscopic examination, *e.g.*, Fig. 4.2(c), did not indicate any entrapped bubbles in the grooves. The oil filling was found to be reliable and is stable for the *LFS*, *e.g.*, compared to the *AFS*. For instance, the surface energy of the *LFS*: $E_{LFS} \sim 0.5 \times \gamma_{pary} + 0.5 \times \gamma_{oil} \sim 32$ mJ/m^2 is an order of magnitude smaller compared to that of the *AFS*: $E_{AFS} \sim r \times \gamma_{pary} \sim 290$ mJ/m^2 with r as the roughness factor (= 6.3, from the ratio of the total area to the projected area[105]). The excellent liquid-interface stability was also considered previously considering surface-immobilized lubricants[106].

Table 4.1 The parameters of the oils (the density: ρ, kinematic viscosity: η, dynamic viscosity: μ, dielectric constant: ε and the surface tension: γ, of the liquids filling the interstices of the liquid filled surfaces (*LFS*).

Oils	ρ **(g/cm^3)**	η **(cm^2/s)**	μ **(mPa·s)**	ε	γ **(mJ/m^2)**
Krytox® 104	1.93	1.77	340	2.1	18
Castor Oil	0.96	3.25	312	4.7	39
Motor Oil 0W-20	0.86	1.19	102	2.4	30
Motor Oil 20W-50	0.86	5.76	495	2.4	30

Setup for measurement of the streaming potential (V_s). The experimental setup is shown in Fig. 4.3(a) with a schematic: Fig. 4.3(b). A microchannel (11.8 cm in length, 9 mm in width, and 255 μm in height), was constituted from a *top surface* (constituted from a polycarbonate coated with silicone), and a bottom *AFS* or *LFS*. These two surfaces are separated by a silicone rubber spacer for sealing and adjusting the height of the channel. For the streaming potential (V_s) measurement, electrolyte, *i.e.*, salt water (in the concentration range of 0.1 mM – 10 mM), preparing by dissolving NaCl into DI water, was pumped by a syringe pump through a tube into the microchannel at a constant flow rate, and provides a pressure gradient. The pressure drop for the experiment was in the range of 200 Pa to 1200 Pa, with lower and higher pressures yielding unreliable values for the V_s. The voltages – related to the V_s, were measured (using a Keithley 2700

Multimeter with input resistance >10 GΩ) through Ag/AgCl electrodes inserted into the two end reservoirs located at the inlet and outlet of the channel. The V_s for each applied pressure was measured six times. Given that the channel length (*L)* and width (*W*) are much larger than channel height (*h*), Poiseuille flow is assumed. The V_s was measured in flow at different orientations with respect to the patterned substrate to consider various tensorial aspects[95,107].

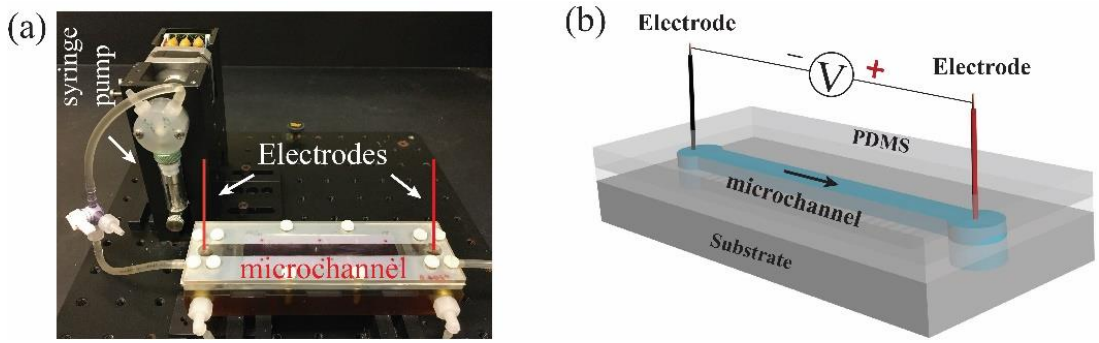

Figure 4.3. The apparatus used for the measurement of the streaming potential, (a) consisting of a syringe pump connected by a tube to the microchannel to provide a constant flow rate to the electrolyte and a pressure gradient, and a (b) schematic of the placement of the electrodes (non-polarizable Ag/AgCl type) at the ends to measure the streaming potential (V_s) related voltage (*e.g.*, the), along the microchannel.

Measurement of the Pressure. The electrolyte flow rate in the channel, constituted from rectangular plate geometry[46], was modulated through a syringe pump: Fig. 4.3(a), and was transduced to an applied pressure (ΔP) based on the Poiseuille relation: $\Delta P = \frac{12\eta LQ}{h^3}$ (Q is flow rate, L is the channel length of ~ 11.8 cm, and h the channel height of ~ 250 μm). The ΔP over the channel length (where the other end was left open to atmosphere) motivated the pressure gradient driven flow. For the experiment, the flow rates were chosen as 0.0275 mL/s (corresponding to 200 Pa), 0.055 mL/s (440 Pa), 0.0825 mL/s (670 Pa), 0.11 mL/s (900 Pa) and 0.1375 mL/s (1130 Pa). Additionally, the calculated pressure drop was checked using a manometer (UEI EM152) by inserting the measurement ports into the two reservoirs of the channel and corresponded very closely to the values estimated from the Poiseuille relation.

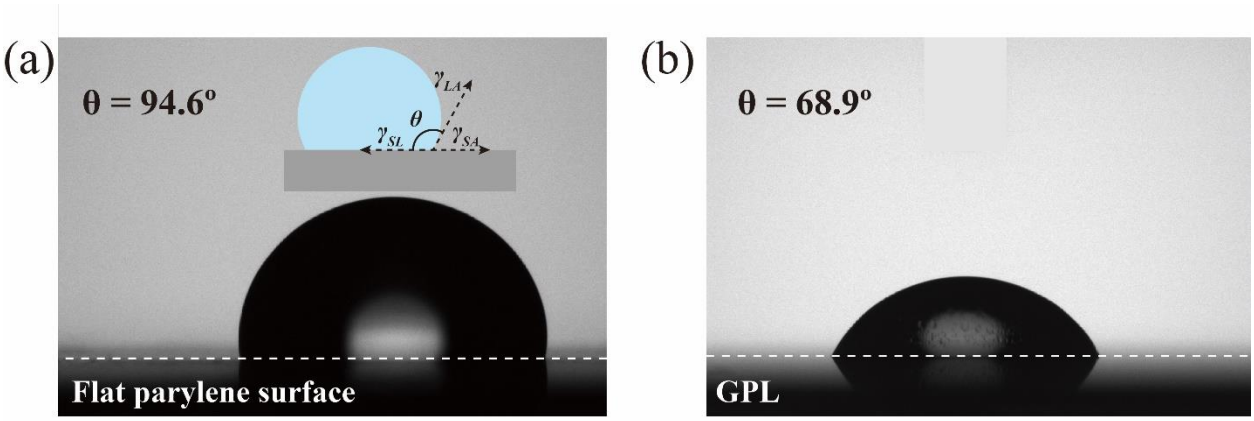

Figure 4.4 The contact angles measured on a (a) water-parylene, and (b) water - GPL 104 interface at ~94.6° and ~ 68.9°, respectively. These values were used for estimating the corresponding γ_{SL} from given γ_{SA} (= 46 mJ/m^2 for parylene) and γ_{LA} (= 72 mJ/m^2).

Table 4.2 The measured contact angles for oils and parylene and calculated interface energy γ_{SL}.

Substrate	**Contact angle**	**γ_{SL} (mJ/m^2)**
Krytox® 104	68.86°	-7.97
Castor Oil	74.39°	19.63
Motor Oil 0W-20	82.93°	21.14
Motor Oil 20W-50	81.01°	18.75
Parylene-C	94.6°	51

Measurement of the contact angle. The electrolyte-oil interfacial energy will influence the interface shape and adhesion force, and modifies the interface flow profile and the V_s. From the Young relation:

$$\gamma_{SA} - \gamma_{SL} - \gamma_{LA}cos\theta = 0 \quad (4.1)$$

with γ_{SA}, γ_{SL}, γ_{LA} as the substrate-air, substrate-liquid and liquid-air surface energy, respectively, θ is the substrate-liquid contact angle. The contact angles of electrolyte (0.1mM NaCl solution) with parylene and Si substrate with different oil films were measured using Ramé-Hart Model 190 Contact Angle Goniometer at 20℃, for estimating the corresponding γ_{SL} from given γ_{SA} and γ_{LA}: Fig. 4.4. The estimated γ_{SL} values for the various oils are listed in Table 4.2 (with γ_{SA} = 46 mJ/m^2 for parylene and γ_{LA} = 72 mJ/m^2).

4.4 Results and discussion

Pressure induced flow on the *LFS*, and related measurement of the streaming potential. We report measurements of the V_s with 0.1 mM electrolyte concentration, where maximal values of the streaming potential were determined: Fig. 4.5. Here, the observed variation arises from the Helmholtz – Smoluchowski relation: $V_s = \frac{\varepsilon\zeta}{\eta\kappa_b}\Delta P$, in terms of the electrolyte dielectric constant (ε), the surface zeta potential (ζ), electrolyte viscosity (η) bulk electrolyte conductivity (κ_b) and pressure drop in the channel (ΔP). Assuming relatively constant ε and η for the electrolyte, the κ_b is proportional to concentration (I) [2,36], while the $\zeta \approx c1 * \log[I] + \mathrm{c2}$ – where c1 and c2 are constants. The overall effect[36] is that the V_s decreases with the I.

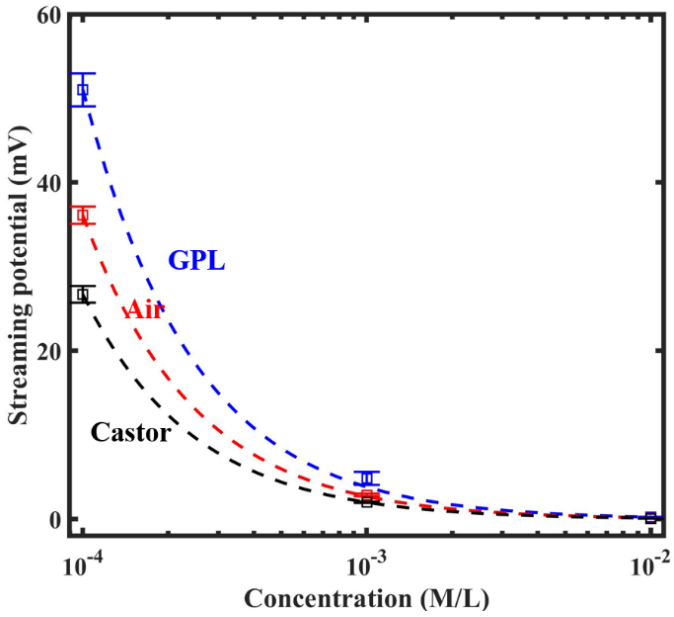

Figure 4.5 Variation of the streaming potential (V_s) for air filled surface (*AFS*), and the GPL oil filled *LFS* and castor oil filled *LFS* at different flowing electrolyte concentrations: *I*, (0.1 mM, 1 mM and 10 mM) at 1200 Pa at transverse direction. The V_s is fit to a relation of the form ~ log $[I]/[I]$ with R^2 = 0.993 for GPL oil filled *LFS*, R^2 = 1 for castor oil filled *LFS*, and R^2 = 1, for the *AFS*.

A typical response of the measured voltage as a function of flow is indicated in Fig. 4.6(a). The voltage increases when the electrolyte was driven through the channel and subsequently attains a steady value V_f. The difference between V_f and the initial voltage: V_0 (in the absence of flow) was defined to be the measured streaming potential: V_s. The variation of the V_s with applied pressure is shown in Fig. 4.6(b) for *both* the AFS and *LFS* (with four different filling liquids) at transverse direction. Generally, a linear variation between the V_s and the ΔP, following the Helmholtz-Smoluchowski relation[32]is observed.

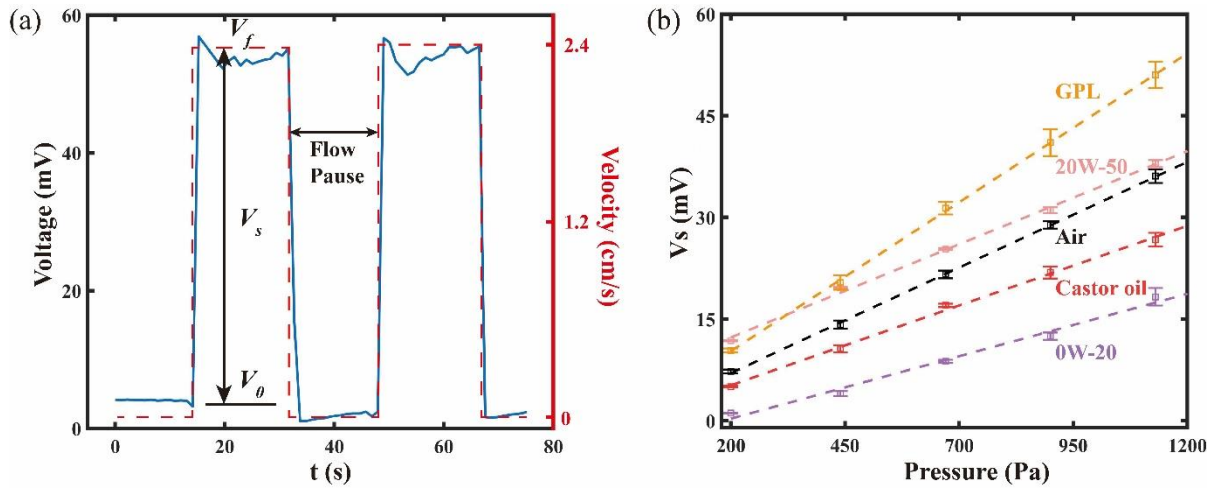

Figure 4.6 (a) A typical measured voltage response indicating the voltage increase under the action of an applied pressure of 1200 Pa causing the flow of 0.1 mM NaCl solution. The periodic action of the syringe pump is responsible for the increase (flow) and decrease (no flow/Flow Pause) of the measured voltage. The corresponding velocity is indicated on the right-hand side. (b) A linear variation of the streaming potential (V_s) as a function of the applied pressure (ΔP), for various filling liquids/oils, in the *LFS*. The GPL is a fluorinated synthetic oil while the 0W-20 and 20W-50 are synthetic motor oils. It is to be noted that a larger V_s is obtained using GPL and other oils compared to air in the interstices, *i.e.*, an air-filled surface (*AFS*).

Possible influence of oils on the measured V_s. The selected oils, which serve as lubricants in the *LFS*, vary in terms of the dielectric constant (ε), dynamic viscosity (η), electrical conductivity (κ), surface tension (γ) and density (ρ) – with the individual properties as listed in Table 4.1. As the V_s may be related to the electrolyte-oil interface shape and influenced by many of such parameters, we first aim to obtain empirical relationships of such an influence through the Buckingham Π theorem[110]. While the given *LFS* system is quite complex, as related to the large number of parameters and the multi-physics aspects, the motivation was to make sense of the results through dimensional analysis. Consequently, at given flowing liquid, groove fraction and groove orientation, one may obtain related non-dimensionalized groups, *i.e.*,

$$\Pi_0 = \frac{V_s}{\eta^{-0.5}\kappa^{-0.5}\gamma} \tag{4.2a}$$

or

$$\Pi_1 = \frac{\rho}{\varepsilon^{-1}\eta^{3}\kappa\gamma^{-2}} \tag{4.2b}$$

may be obtained. From fitting the above, with V_s from experiment and the values of oil properties, an empirical relationship $\Pi_0 = F(\Pi_1)$ and fit ($R^{\wedge 2} \sim 0.82$) was obtained: Fig. 4.7. A larger (/smaller) ϕ_{oil} may be expected to increase (/decrease) the polarizability and increase (/decrease) friction at the oil-water interface[1] and yield a decreased (/enhanced) V_s. A possible correspondence between the η and the ε_r was indicated earlier[111].

For a better understanding of the obtained V_s variation, we considered the flow profile variation for an *LFS* taking into account *both* the electrical attributes, such as ε, κ, as well as the nominal fluidic parameters, such as the ρ, η, and γ, of both the impregnated liquid in the *LFS* as well as at the electrolyte – *LFS* interfaces.

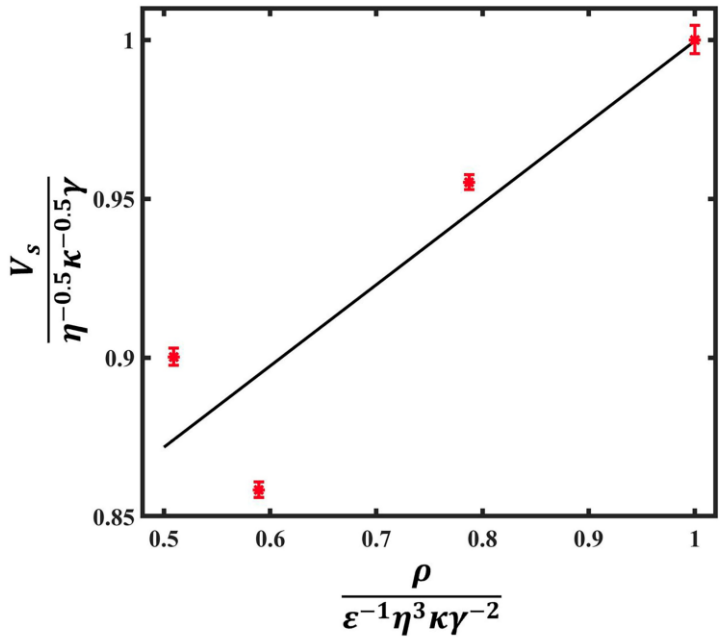

Figure 4.7. Experimentally derived correlations between the obtained streaming potential (V_s) on *LFS* as a function of non-dimensional parameters, through considering the viscosity (η), electrical conductivity (κ), surface tension (γ), the density (ρ) and the dielectric constant (ε) of the filling liquid.

The influence on slip, as a function of electrical parameters of the filling liquid, in *LFS*. One manifestation of a liquid impregnated surface, akin to the *LFS* discussed in this work, was a slippery liquid infused porous surface[27]. There, the wettability in terms of enhancing the liquid slip was considered. The

slip length (b), as determined through the slip velocity (u_s) and the surface shear rate ($\frac{\partial u}{\partial y}|_{y=0}$) from Navier boundary condition: $u_s = b\frac{\partial u}{\partial y}|_{y=0}$, would be dependent on the filling liquid properties[99,104]. Considering electrical characteristics, we indicate the inverse relation of the V_s to the dielectric constant of oil: ε_{oil}. For a hybrid surface, such as the LFS, consisting of both solid parylene and liquid oil, an effective slip length b_{eff} may be defined.

Using the relations in Belyaev & Vinogradova[112] and Nizkaya[113] *et al*, we calculated the slip length of the *LFS* with transverse grooves where we consider the groove orientation, groove fraction and viscosity ratio. The local slip length for transverse groove, considering the viscosity of the electrolyte (η_{elect}) and the oil (η_{oil}) and a geometry-dependent function: β, was estimated through[113]:

$$b = w\frac{\eta_{elect}}{\eta_{oil}}\beta \tag{4.3}$$

For deep grooves, as in our case (with a height: h of ~ 95 μm, and a width: w of 18 μm, *i.e.*, with $h/w \geq 1$), $\beta \approx 0.12$. The effective slip length (b_{eff}) was then estimated to be:

$$b_{eff} = \frac{L}{2\pi}\frac{\ln\left[\sec\left(\frac{\pi\phi}{2}\right)\right]}{1+\frac{L}{2\pi b_l^y}\ln\left[\sec\left(\frac{\pi\phi}{2}\right)+\tan\left(\frac{\pi\phi}{2}\right)\right]} \tag{4.4}$$

The calculated b_{eff} (/b) for GPL oil and castor oil filled *LFS* are then ~ 2.5 nm (/6.4 nm) and ~ 2.7 nm (/6.9 nm), respectively. The b_{eff} /b ratio is then ~ 0.4, corresponding closely[114] to the expected value of ~ 0.5 (the area fraction), when $b/L \ll 1$, $b_{eff}^{\perp,\parallel} \simeq \phi b$. If we consider the charge effects at the gas/oil sectors on flow transport[114], then the electroosmotic mobility for transversely oriented groove was shown to be:

$$M_{\perp} = \frac{\varepsilon\zeta}{\eta}\left[1+\frac{b_{eff}}{b}\left(\frac{q_2}{q_1}(1+kb)-1\right)\right] \tag{4.5}$$

From literature, the surface charge density is ~ -3.6 mC/m^2 (= q_1) for parylene[51] and ~ -1.8 mC/m^2 (=q_2) for oil[74]. Through V_s measurements on flow of 0.1 mM NaCl solution (with k ~ (1/30) nm^{-1} $= 1/\lambda_D$, where λ_D is the Debye length) on parylene and PDMS coated *flat* substrates, and $V_s = \frac{\varepsilon\zeta}{\eta\sigma}\Delta P$, we estimated

that $\zeta_{parylene}$~31.7 mV and ζ_{PDMS}~26.9 mV .Then, the *enhanced* zeta potential for bottom surface $\zeta_{bottom,en}$, considering the correspondence[114,115] of the electroosmotic mobility to the V_s is:

$$\zeta_{bottom,en} = \zeta_{bottom}[1 + \frac{b_{eff}}{b}\left(\frac{q_2}{q_1}(1 + kb) - 1\right)] \tag{4.6}$$

and the concomitant ζ for the channel is:

$$\zeta_{channel} = 0.5\zeta_{PDMS} + 0.25\left(\zeta_{parylene} + \zeta_{oil}\right)\left[1 + \frac{b_{eff}}{b}\left(\frac{q_{oil}}{q_{parylene}}(1 + kb) - 1\right)\right] \tag{4.7}$$

Here, the effective zeta potential of the rectangular channel was defined through $\zeta_{eff}(= \frac{1}{2}\zeta_{bottom} + \frac{1}{2}\zeta_{top})$, and for the ζ_{bottom}, a weighted summation[94] of $\zeta_{parylene}$ and ζ_{oil} was assumed. We then estimate that ζ_{GPL} ~ 214 mV and ζ_{castor} ~ 66 mV from the above relation. The larger V_s obtained with the use of GPL oil in the *LFS* compared with that of the use of castor oil could be tentatively ascribed to the larger ζ_{GPL}.

It may also be necessary to consider the issue of *fixed* charges and *mobile* charges on the slipping interfaces[109]. In Maduar[109], *et al*, a parameter μ was used to modify the Navier slip boundary conditions, with μ =0 for fully *mobile* charges and with μ = 1, for *fixed charges*. If there is adsorption of hydroxyl ions, for example, the liquid-oil interface would be charged, and correspondent V_s is modified to:

$$V_s = \frac{\varepsilon\zeta}{\eta\sigma}(1 + \mu b_{eff}k)\Delta P \tag{4.8}$$

Consequently, another reason for the difference in the V_s between GPL- and castor oil- filled *LFS* may be due to differing μ, and that $\mu_{GPL} > \mu_{castor}$ - due to the smaller dielectric constant of GPL oil (ε~ 2.1) compared to castor oil (ε~ 4.7). Considering the continuity of tangential shear stress across the electrolyte (with η of ~ 1 mPa·s) - oil (with η of ~ 300 mPa·s) interface, it was assumed that the slip is along the oil-electrolyte interface.

An alternate understanding of the influence of charges, may be manifested through a charge density (σ) difference: $|\sigma_{parylene} - \sigma_{oil}|$, which is expected to yield a longitudinal electric field (E_x) as well as a transverse electric field (E_y), the former of which drives ion motion across the surface: Fig. 4.8. Here, where x is in the direction of fluid flow and the and y is the orthogonal direction- transverse to the direction of the pressure driven flow. It may be expected that with a large (/small) σ_{oil}, that the screening of the charge into the flowing electrolyte occurs over a smaller (/larger) distance yielding a larger (/smaller) ρ_s and ζ. The shear plane is then closer (/further), implying smaller (/larger) u_s and b. We estimated, for the parylene coated Si surface: $\sigma_{parylene}$ at - 3.6 mC/m^2 and that of the oil: σ_{Oil} at – 1.8 mC/m^2. The resultant E_y would be of the form: $E_{y,\,parylene} \sim \sigma_{parylene} / \varepsilon_{elec}$ and $E_{y,\,oil} \sim \sigma_{oil} / \varepsilon_{elec}$, respectively. If we assume no residual charge at the oil-electrolyte (*elec*) interface, then from the continuity of electrical displacement and electrical fields, across the interface: (i) $\varepsilon_{oil} E_{y,\,oil} = \varepsilon_{elec} E_{y,\,elec}$, and (ii) $E_{x,\,oil} = E_{x,\,elec}$. Here, the capillary number (Ca) = $\eta v/\gamma$, with η the dynamic viscosity, v as the characteristic velocity, and the surface tension (γ), was estimated to be of the order of 10^{-3}, which indicates that the surface tension dominates over the viscous forces. A similar inference could be made through estimating the Bond number (Bo) – which relates the difference of the density of the two phases (electrolyte and oil) over a characteristic length, say, the groove width, with respect to the surface tension. Consequently, the pressure driven flow induced viscous force will not significantly deform the liquid-liquid interface[116].

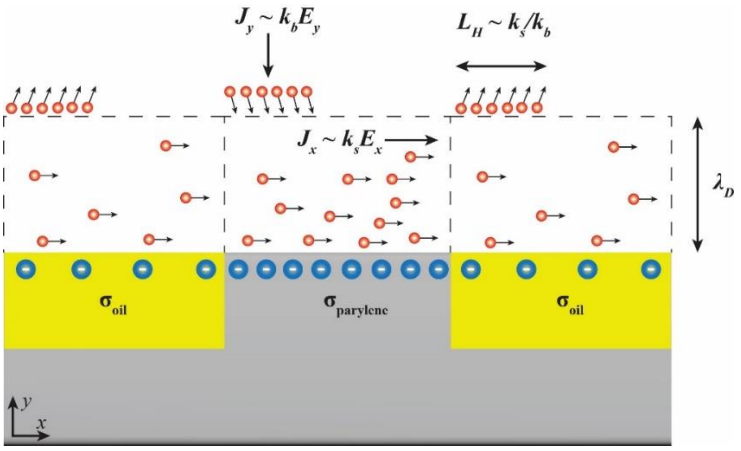

Figure 4.8 The schematic of electrokinetic flow over *LFS* surface with varying surface charge density (σ). As σ_{oil} is less than $\sigma_{parylene}$, the surface conductivity κ_s is smaller for the oil regions. Consequently, driven surface currents: J (both parallel: in the x-direction, and perpendicular: in the y-direction, to the *LFS*) serve to enhance the slip and the slip length (b). The b was correlated to the healing length $L_H \sim \kappa_s/\kappa_b$ (the ratio of the surface to the bulk electrical conductivities), the Debye length (λ_D), η_{elec}, as well as the ε_{oil} and σ_{oil}, through analysis and experiment.

The deployment of a *hybrid* bottom surface, constituted from both the liquid and the solid with the concomitant differing surface charge densities may be expected to yield concentration polarization[44] as well as non-uniform conduction[117] effects over the surface. In electroosmotic flows, the ions contributing to the surface current ($J_x \sim \kappa_s E_x$, with κ_s being the surface conductivity) in the direction of the flow are replenished through an ion current from the bulk liquid (of conductivity: κ_b) over a length scale (termed a healing length: L_H) and due to a normal component of the electric field (E_y). From such ion conservation considerations: $\kappa_s E_x \sim \kappa_b E_y L_H$. If E_x and E_y are of comparable magnitudes, then the L_H is of the order of κ_s/κ_b.

For flow over the LFS, it may be expected that the E_x or the E_y may contribute to u_s and the resultant surface current: $J_{s,x} \sim \rho_s u_s$, where ρ_s is the *mobile* surface charge density. From analogy to the arguments presented above, for E_y induced current dominated case, $\kappa_b E_y L_H \sim \rho_s u_s$, implying, for a given shear rate ($\partial u/\partial y$) in the absence of nonlinear effects[6]:

$$b \sim \frac{\kappa_b \sigma_{oil} L_H}{\varepsilon_{elec} \rho_s} \tag{4.9a}$$

However, this relation can not explain the experiment results that the slip length is larger for filled oil with smaller dielectric constant. Alternately, if the longitudinal electrical fields, say $E_{x,\,elec}$ (=$E_{x,\,oil}$) are more responsible for the fluid slip, then $\kappa_s E_{x,\,elec} \sim \rho_s u_s$, indicating:

$$b \sim \frac{\kappa_s \sigma_{oil}}{\varepsilon_{oil} \rho_s} \tag{4.9b}$$

Here, a larger b or a u_s also seems to be facilitated through a higher σ_{oil}. Additional electrostatic considerations, *e.g.*, related to the screening in the electrolyte, must also be considered. It was previously indicated, for instance[74], that the magnitude of the associated surface charge density may be independent of oil type, and mostly dependent on the aqueous phase/electrolyte. Indeed, testing with several oils indicates that the correlations indicated in Eqns. 4.2(a) and 4.2(b), are valid. As we use non-polar oils in the *LFS*, the molar conductivity is negligible and the Walden rule relating η to the σ is not applicable[118].

At the shear plane, from considering an equivalence of the shear stress: τ ($\sim \eta\, \partial u/\partial y$) to u_s, a direct correlation between the b and the η of the electrolyte may be deduced. Indeed, such a correlation and scaling has been previously indicated for liquid slip on air[119], through a "gas cushion" model[29]. From the previously deduced $b \sim 1/\varepsilon_{oil}$, we now obtain a significant correlation for the oil-electrolyte interface, that:

$$b \sim \frac{\eta_{elec}}{\varepsilon_{oil}} \tag{4.10}$$

The expression above posits a relation between the measured V_s and the flow characteristics as modulated by the oil-electrolyte interface/s in the *LFS*. Consequently, aspects of the surface that promote b, *e.g.*, geometry[29], air bubbles[6], surface interactions, *etc.*, may all now be utilized for obtaining enhanced V_s.

4.5 Conclusion

In summary, we have indicated that enhanced streaming potentials (V_s) may be obtained through electrolyte flows over liquid filled surfaces. It was observed that the V_s was sensitive to the character of the

liquid, in terms of the density viscosity, dielectric constant, in the *LFS.* Moreover, the magnitude and variation of the pressure at the ridge-groove interface seems to be important in determining the enhancement of the V_s over that obtained in air-filled grooves and surfaces. The influence of such local perturbations merit further study, *e.g.,* the modification of the flow profile close to *LFS* surface[120], due to the unequal interface energy between electrolyte-parylene (*ridge*) and electrolyte-oil (groove)**.** A correlation of the slip length (*b*) to the V_s yields a better understanding of the hydrodynamics inherent in electrokinetic flows. The presented study indicates a path forward[94] in terms of generating large streaming potentials, through fluid flow in microchannels with a *hybrid* surface – consisting of both solid and oil interfacing with an aqueous electrolyte, moving beyond smooth walled nanoscale channels[46]. Our results and those expected from extending our investigations may be utilized to gain greater insights with applications ranging from energy conversion[46,66,83,85,87] to transport in lab on a chip devices[59,60] and nanosystems[121].

4.6 Acknowledgement

This chapter, in full, is a reprint of the materials as it appears in Fan, B. and Bandaru, P.R., Modulation of streaming potential and slip characteristics in electrolyte flow over liquid-filled surfaces, Langmuir, 2019, 35, 18, 6203 – 6210.The dissertation author was the primary investigator and author of this paper. The authors are grateful for support from the National Science Foundation (NSF: CBET 1606192). We also appreciate the assistance of Prof. J. Friend and P. Chen for help with imaging.

Chapter 5 Tensorial Modulation of Electrokinetic Streaming Potentials on Air and Liquid Filled Surfaces

5.1 Abstract

Textured surfaces, comprised of grooves filled with air, e.g., air-filled surfaces (*AFS*), or with liquid, e.g., liquid-filled surfaces (*LFS*), significantly influence fluid flows and the related electrokinetic streaming potential (V_s). Here, electroosmotic mobility related tensorial effects on the V_s were experimentally investigated. A significant modulation of the V_s, as high as 100%, due to transverse pressure gradients, was demonstrated. The study yields insights into understanding geometrical effects in electrolyte flows with implications to the establishment of local electric fields, energy generation, and biological separations.

5.2 Introduction

Electrokinetic flows, considering the movement of electrolyte relative to another charged surface, are important for understanding the effects of charge accumulation and dispersion with applications ranging from power generation[83–85] to biochemical separations[31,86]. There are two major related phenomena in such flows, under a pressure difference across the microchannel, *i.e.*, (i) where the motion of ions in the electrical double layer (EDL) near a charged surface generates an electrical streaming current (I_s), and (ii) under open-electrical circuit conditions – where a potential difference, termed the streaming potential (V_s) is measured, due to charge separation. The V_s may be particularly enhanced in micro- and nano-scale fluidics[46,83,89], *e.g.*, through using through the overlap of EDLs in nanometer size pores/channels which may enable unipolar flow and new battery-like voltage sources. Our group has pioneered the use of liquid filled surfaces (*LFS*) to simultaneously enhance the V_s as well as to reduce frictional drag[100,101,123] between the flowing electrolyte and the surface. Here, the hydrophobic character of the *LFS* enhances flow, through inducing a finite slip

velocity[66], and reduces the potential drop that contributes to a reduction of the V_s. Going beyond such preliminary measurements, we discuss in this work, how the *AFS*/*LFS* geometry especially the groove orientation, may be related to the changes in the V_s, which has been typically considered through the Helmholtz-Smoluchowski (H-S) equation, and derived on homogeneous surface[8,36]:

$$V_s = \frac{\varepsilon\zeta}{\eta_e\sigma}\Delta P \tag{5.1}$$

Here, ε ($= \varepsilon_o\varepsilon_r$, with ε_o=8.854·10^{-12} C^2/Nm^2 is the vacuum permittivity and $\varepsilon_r$is the relative permittivity) is the permittivity of the electrolyte, ζ is the zeta potential of the surface, η_e is the electrolyte viscosity, and σ is the electrolyte conductivity. Relevant to SH surfaces[5] is an enhanced ion mobility[32], M= $\frac{\varepsilon\zeta}{\eta_e}$, predicated on the requirement[94,96,124] that the surfaces ensuring fluid slip have a significant charge density with a similar magnitude and sign as that of the no-slip surface. However, when the surface is uncharged/partially charged, the magnitude of the V_s could be diminished compared to a homogeneously charged smooth surface [94,124], as was also confirmed through our own experimental work. The *LFS* also serve to circumvent the ambiguity related to electrolyte-air interfaces through filling liquid (of a definite ε_r) into the interstices of patterned surfaces (Figure 5.1) and ensure a definitive charge density. While preliminary experiments stated that a 50% enhancement in the V_s over the use of traditionally used air-filled surfaces (*AFS*) could be obtained, such improvement seems to hinge critically on the physico-chemical attributes of the filling liquid[125], as well as on geometrical parameters such as the orientation of the surface with respect to the applied pressure gradient.

Typically, the influence of geometrical parameters of the substrate has been considerably discussed in the context of wetting[1], *e.g.*, with respect to anisotropy[105], as well as its influence[30] on the slip length (*b*), *e.g.*, the relative variation for stripe and post geometries[29]. A generalization of the underlying concepts to describe surface anisotropy through slip and related interfacial mobility tensors[107] has yielded insights into

the modulation of flows, say, on hydrophobic surfaces[112]. Considering that the electroosmotic mobility (*M*) may also be formulated as a tensor, insights into charged liquid flows on heterogenous geometries[115] were obtained into electroosmotic slip, with respect to modification of fluid flow patterns, such as flow reversal[114]. The degree of alignment of the texture, *e.g.*, misaligned grooves, was shown to generate transverse shear, also leading to complex flow patterns and mechanisms for mixing in directions transverse to the nominal pressure driven flow axes[126]. All such intriguing characteristics of flow have been studied from a theoretical and computational perspective and are subject to experimental verification. Moreover, the specific impact of such tensorial generalizations, *e.g.*, of the *b* and *M*, have not been discussed with respect to their influence on the V_s. In this paper, we first report and discuss the modulation of the V_s brought about through groove orientation variation of the substrate and studied the rotation angle at which yielded the smallest V_s.

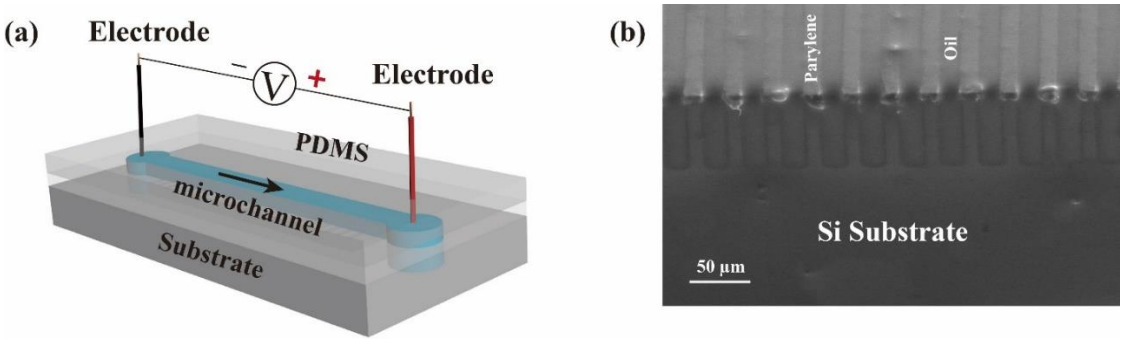

Figure 5.1 (a) Electrolyte flow (driven through a syringe pump yielding a pressure gradient) in a microchannel generates an electrokinetic streaming potential (V_s) that may be measured by a voltmeter. The patterned parylene substrate either has air in the grooves, i.e., an air-filled surface (*AFS*), or (b) liquid in the grooves, i.e., a liquid filled surface (*LFS*), SEM image.

5.3 Methods

Fabrication of Geometrically Textured Surfaces. The groove patterned *AFS/LFS* used in the experiment was fabricated by photolithography and have been previously reported in chapter 3 and 4. Here, we report on the obtained results from surfaces constituted from a given groove width, w, groove period, L (= d + w), with d as the lateral length of the solid surface, oriented at an angle θ (in the range of −90° to 90°), with respect to the flow induced by an applied pressure gradient: Figure 5.2, also see right bottom

inset to Figure 5.3(a). Here, θ is the rotation angle needed to align the coordinate axes (x, y) fixed on the *AFS* or *LFS* to the coordinate axes oriented to the frame in which the liquid electrolyte is flowing (x′, y′) due to a uniaxial pressure gradient, as indicated in the bottom right inset to Figure 3(a). For sample groove orientation parallel to the flow, θ = 90°, while for groove orientation transverse to the flow, θ = 0°. The air fraction, ϕ_a = w/L. For the *LFS*, the grooves were filled (replacing the air) with oils (e.g., Dupont Krytox GPL 104 and castor oil) of low surface energy and immiscible with the aqueous electrolyte (NaCl in deionized water). We ensured the robustness of the *LFS*, i.e., preventing the drainage of the filling liquid under external shear flow[127] through visual examination of the interface[125]. Moreover, it was previously noted that the filling liquid could be retained indefinitely in the grooves if L was less than a critical length[127]: L∞. As for the tested experimental conditions, the L∞ was estimated to be of the order of millimeters.

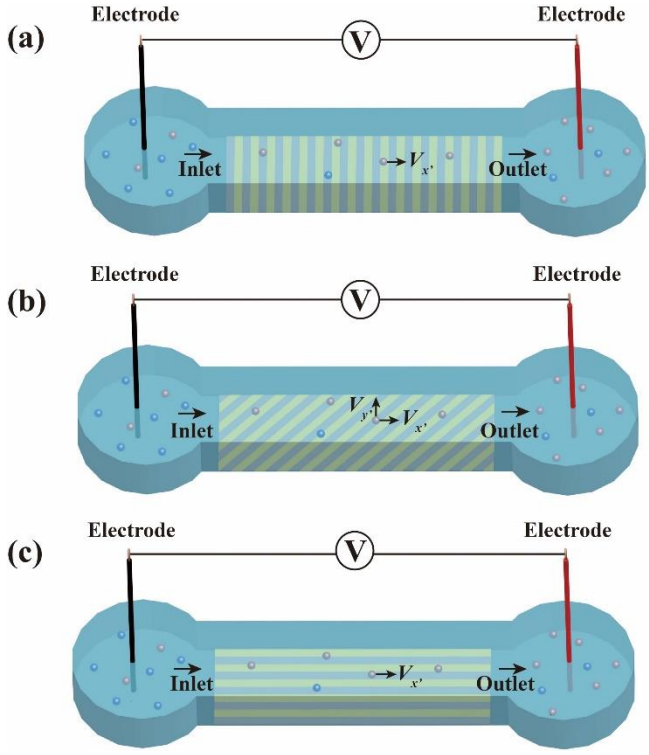

Figure 5.2 Differing orientation of the grooves with respect to the flow (from left to right). The grooves are oriented (a) perpendicular to the flow (θ = 0°, top), (b) parallel to the flow (θ = 90°, bottom), or (c) at an intermediate angle (θ = 45°, middle). The voltages are measured in the horizontal (i.e., through $V_{x'}$) and vertical (i.e., through $V_{y'}$) directions.

Measurement of the Streaming Potential. The V_s experiments were carried out through the measurement of the voltage under the flow of electrolyte at a constant flow rate, driven by an applied pressure difference (ΔP), using a setup as in the schematic of Figure 5.1(a). Electrolyte (typically, NaCl dissolved in water) of concentration 0.1 mM (chosen for obtaining reliable and maximal Vs) was flowed into the microfluidics chamber (of length ~11.8 cm, width ~0.9 cm, and height ~255 μm) using a syringe pump. Poiseuille flow conditions were assumed for converting the flow rate to an equivalent pressure. The differential pressure was in the range of 200 to 1200 Pa and was calibrated using a manometer (UEI EM152). The chosen range of pressure yielded stable and reproducible Vs in the microchannel. The channel surfaces were constituted from an upper surface (silicone coated onto polycarbonate) and a bottom test surface, which was of the *AFS* or the *LFS* type. More experimental details on the voltage measurement and flow arrangement have been previously discussed in chapter 3 and 4. The V_s was measured six times at each applied pressure and the average value was used.

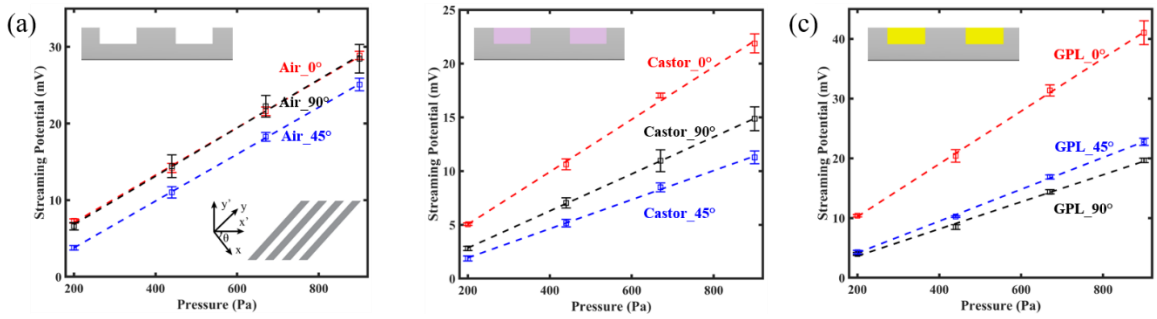

Figure 5.3 Measured streaming potential (V_s) over an (a) *AFS*, (b) castor oil filled *LFS*, and (c) GPL oil filled *LFS*, as a function of applied pressure, at three different orientations of the grooves with respect to the flow. The dotted lines are a guide to the eye and connect the measurements. The top left insets in panels a−c are a schematic of the grooves. The bottom right inset of (a) defines the θ, the rotation angle needed to align the coordinate axes (x, y) fixed on the *AFS/LFS* grooves to the coordinate axes oriented to the frame in which the liquid electrolyte is flowing (x′, y′). While the $V_s(\theta = 0°)$ is generally larger for all the *AFS* and *LFS*, each panel (a−c) represents different relative variation of the V_s at θ = 45° and θ = 90°.

5.4 Results and Discussion

We consider the anisotropy of electrokinetic effects through the electroosmotic mobility tensor ***M*** (which is related the ratio of the streaming potential gradient/related electric field: ***E***, to the pressure

gradient $\Delta \boldsymbol{P}$). *i.e.*, $\boldsymbol{E} = -\boldsymbol{M}\frac{1}{\sigma}\Delta \boldsymbol{P}$. Considering θ as the rotation angle needed to align the coordinate axes (x, y) fixed on the *AFS* or *LFS* with respect to the axes parallel (x') and perpendicular (y') to the flow direction - as indicated in Figure 5.3, we obtain[128,129]:

$$\boldsymbol{M'} = \begin{bmatrix} M_x cos^2\theta + M_y sin^2\theta & (M_x - M_y) sin\theta cos\theta \\ (M_x - M_y) sin\theta cos\theta & M_y cos^2\theta + M_x sin^2\theta \end{bmatrix} \tag{5.2}$$

We then obtain the electric field in the x' direction as:

$$E_{x'} = -\frac{1}{\sigma}\left[\left(M_x cos^2\theta + M_y sin^2\theta\right)\frac{dP}{dx'} + \left(M_x - M_y\right) sin\theta cos\theta \frac{dP}{dy'}\right] \tag{5.3}$$

The corresponding V_s, over a groove period (L), is the corresponding integral of the $E_{x'}$:

$$V_s = \int_0^L \frac{1}{\sigma}\left[\left(M_x cos^2\theta + M_y sin^2\theta\right)\frac{dP}{dx'} + \left(M_x - M_y\right) sin\theta cos\theta \frac{dP}{dy'}\right] dx' \tag{5.4}$$

For instance, at representative values of θ, we obtain:

$$V_s(0°) = \int_0^L \frac{1}{\sigma} M_x \frac{dP}{dx'} dx' \tag{5.5a}$$

$$V_s(45°) = \int_0^L \frac{1}{\sigma}\left[\frac{1}{2}\left(M_x + M_y\right)\frac{dP}{dx'} + \frac{1}{2}\left(M_x - M_y\right)\frac{dP}{dy'}\right] dx' \tag{5.5b}$$

$$V_s(90°) = \int_0^L \frac{1}{\sigma} M_y \frac{dP}{dx'} dx' \tag{5.5c}$$

Several interesting aspects are evident through Eqns. 5.2 - 5.4, *e.g.*, the use of a pressure gradient implying[128] components of both longitudinal and transverse to the flow direction - from tensorial considerations, the fluid flux transforms covariantly[130], *i.e.*, in the same way as the basis vectors, aligning the flow with the grooves[131]. Due to the existence of the side walls of the channel, the consequent recirculation[128,131] yields transverse components, with either positive/negative gradients $\frac{dP}{dy'}$. Since the experimental applied pressure is along x', the generated transverse $\frac{dP}{dy'}$ will be positive. From an

electrokinetic point of view, only when M_x=M_y, would the off-diagonal terms in Eqn. 5.2 be zero and yield a V_s (θ = 45°) as the arithmetic mean of the V_s obtained for θ = 0° and θ = 90°. For instance, we obtain:

$$\frac{1}{2}[V_s(0°) + V_s(90°)] - V_s(45°) = -\frac{L}{2\sigma}(M_x - M_y)\frac{dP}{dy'} \tag{5.6}$$

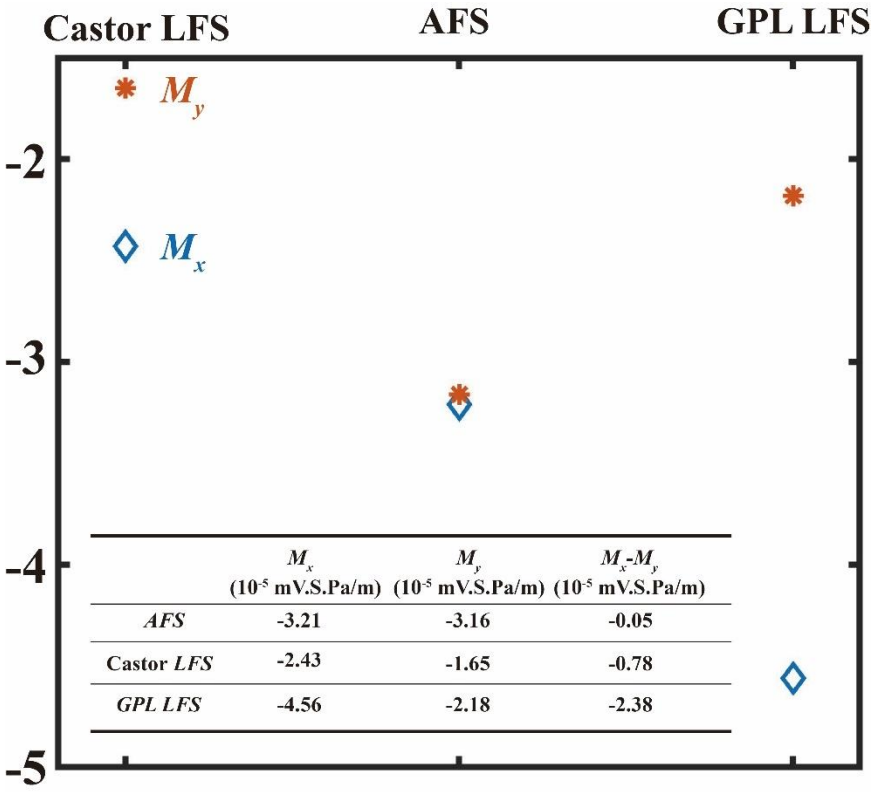

	M_x (10^{-5} mV.S.Pa/m)	M_y (10^{-5} mV.S.Pa/m)	M_x-M_y (10^{-5} mV.S.Pa/m)
AFS	-3.21	-3.16	-0.05
Castor *LFS*	-2.43	-1.65	-0.78
GPL LFS	-4.56	-2.18	-2.38

Figure 5.4 Calculated eigenvalues of the electrokinetic mobility tensor (***M***), i.e., M_x and the M_y, see Eqn. 5.2 in the text, estimated from streaming potential (V_s) measurements for an *AFS*, castor oil filled *LFS*, and GPL oil filled *LFS* (at 0.1 mM electrolyte concentration, σ = 0.001 S/m, $\frac{dP}{dx'}$ = 7627 Pa/m).

Such considerations may be used to explain the related experimental observations in Figure 5.3. The estimates of the M_x and the M_y were estimated experimentally through measuring the streaming potential for two orientations of the grooves with respect to the flow direction, *i.e.*, M_x from V_s (θ = 0°) using Eqn. 5.5(a), and M_y from V_s (θ = 90°) using Eqn. 5.5(c). The respective values are listed in Figure 5.4. Since $M_x - M_y$ is negative, $\frac{dP}{dy'}$ is positive, the V_s of 45° is smaller than the arithmetic mean of that of 0° and 90°.

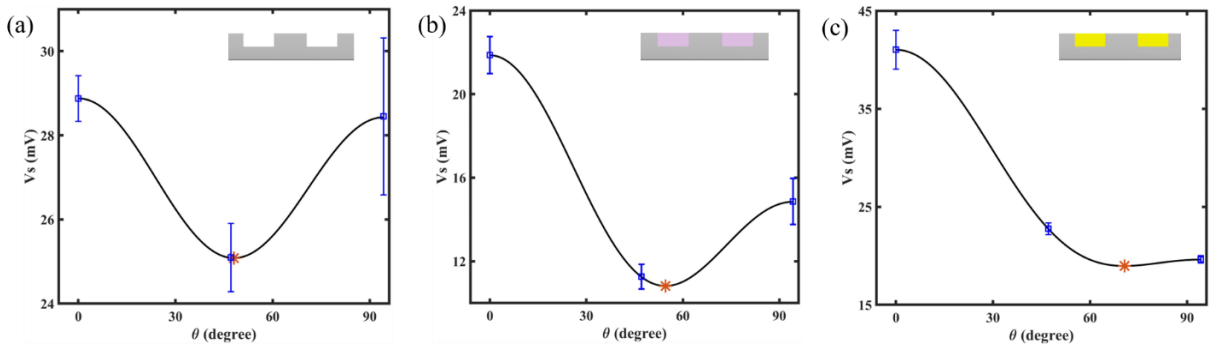

Figure 5.5. Variation of the V_s with groove orientation angle (θ) for (a) an *AFS* ($\theta_{min} \approx 45.9°$ with corresponding $V_{s,min} \approx 25.1$ mV) (b) castor oil filled *LFS* ($\theta_{min} \approx 52.2°$ with corresponding $V_{s,min} \approx 10.8$ mV), and (c) GPL oil filled *LFS* ($\theta_{min} \approx 67.5°$ with corresponding $V_{s,min} \approx 18.9$ mV). The V_s was measured at 900 Pa with the flow of 0.1 mM NaCl. Tensorial effects and transverse pressure gradients were invoked to explain the observed variations and the theoretical Vs minima (orange star).

Actually, $\frac{dP}{dy'}$ is a function of θ and is in the form[128] of $\frac{dP}{dy'}(\theta) = c * sin\theta cos\theta$. The values of $\frac{dP}{dy'}$ at 45° was estimated using Eqn. 5.6, based on the obtained values of M_x and M_y and the measured V_s at $\theta = 0°$, 45° and 90°, and $\frac{dP}{dy'}(\theta)$ could be obtained. The dependence of V_s on θ was derived via plugging $\frac{dP}{dy'}(\theta)$ into Eqn. 5.4. It was observed that the variation of the V_s (θ) seems to exhibit a minimum, say at θ_{min} shown in Figure 5.5. From Figure 5.4, Eqns. 5.4 and 5.5, and a negative $\frac{dP}{dx'}$ (as the pressure decreases in the flow direction), it may be deduced that such variation would essentially arise from the $\frac{dP}{dy'}$ term – which may be negative or positive and is dependent on θ. It was found that the θ_{min} was less sensitive to a change of M_x or M_y but is decreasing with $\frac{dP}{dy'}$ and is set to 45° when $\frac{dP}{dy'}$ is large enough, and $V_s(\theta)$ exhibits a $sin^2(2\theta)$ form. This is because that the $V_s(\theta)$ is composed of the diagonal term contribution and off-diagonal term contribution. The diagonal term in equation (5.5) is $\int_0^L [\frac{1}{\sigma}(M_x cos^2\theta + M_y sin^2\theta)\frac{dP}{dx'}]dx'$ which monotone decreases with θ, while the off-diagonal term $\int_0^L [\frac{1}{\sigma}(M_x - M_y) sin\theta cos\theta \frac{dP}{dy'}]dx'$ is minimum at θ = 45°. When the magnitude of $\frac{dP}{dy'}$ increases, the off-diagonal term will become more dominant, and θ_{min} will approach to 45° with increasing $\frac{dP}{dy'}$.

5.5 Conclusion

In summary, we have indicated geometrically induced modulation of the V_s obtained through electrolyte flows over specifically oriented air and liquid filled surfaces, described through tensorial considerations. Such engineering could find application in the establishment of local potentials and electric fields. Further experiments on electrolyte flow in microchannels with engineered hybrid surfaces would yield insights into electrokinetics beyond smooth walled channel flow. Such tunability of the V_s arises may be related to a variation in the local and effective slip characteristics as well as the surface charge density of the *AFS* and *LFS* and the presented work offers new avenues into exploring such effects. Moreover, related investigations would yield insights into the generation of transverse pressure gradients due to anisotropic surfaces, surface heterogeneities and roughness, with implications to the efficiency of energy conversion and lab on a chip devices.

5.6 Acknowledgement

This chapter, in full, is a reprint of the materials as it appears in Fan, B. and Bandaru, P.R., Tensorial modulation of electrokinetic streaming potentials on air and liquid filled surfaces, Langmuir, 2019, 35, 46, 14812 – 14817. The dissertation author was the primary investigator and author of this paper. The authors are grateful for support from the National Science Foundation (NSF: CBET 1606192). We also appreciate the assistance of Prof. J. Friend and P. Chen for help with imaging.

Chapter 6 Future Work

Though there is a long history for electrokinetics, the development of micro/nano fabrication makes electrokinetic phenomenon revive and there are still a lot to be investigated, both in fundamental research and practical application. Especially, the electrokinetics on liquid-filled surface is a quite new multi-physics coupling phenomenon, which make it worthy to continue to study this phenomenon. Here, I proposed the following future directions.

Influences of geometrical factors of liquid-filled surfaces on V_s. The geometrical parameters, such as groove width, groove depth and groove fraction, play an important role in tuning the fluid slip characters and zeta potential (ζ) of LFS, which will influence the generated V_s. I tried to vary the groove width, groove depth and groove fraction with different values and measured the corresponding V_s. Generally speaking, the V_s of LFS increases with groove depth and decreases with groove width and groove fraction. However, it is difficult to find a quantitative relationship between the measured V_s and these geometrical parameters. In the future, simulation and theoretical analysis will be performed to find the quantitative relationship.

Electrokinetics on LFS with 2D pattern. Till now, all the work on electrokinetics on LFS focused on the 1D groove geometry. 2D geometries, such as post and hole geometry, have different fluid slip characteristics compared with groove pattern. For example, the fluid slip for strip geometry scales with solid fraction as[29] $b_{strip} \sim -Llog(\phi_s)$, while the post geometry scales as[29] $b_{post} \sim \frac{L}{\sqrt{\phi_s}}$. In addition, the interfacial fluid dynamics and robustness of the LFS will also be changed. In post geometry, the filled oil in the interstices will be interconnected and can flow in two directions, while for hole geometry, the filed oil inside the holes will be isolated and confined in the holes. The difference in oil movement between groove, post and hole geometries will greatly influence the electrolyte slip, electrolyte-oil interface

dynamics, the robustness of LFS and the induced electrokinetics. In the future, expansion to electrokinetics on LFS with 2D geometry will be performed both experimentally and theoretically to investigate the corresponding fluid slip, streaming potential, etc, and those results will be compared with those of 1D geometry.

Nanoscale electrokinetics. I have pioneered in studying electrokinetic flow in microscale in my Ph. D period. The nanofluidic phenomena will be far different from microscale flow due to the dominant surface force effects and electrical double layer overlap. Nano electrokinetics is important in energy conversion, single molecule analysis and water purification. It may be possible to obtain voltages of the order of 1 volt through the use of nanoscale fluid channels. The fluid transport in *LFS* composed nanochannel and interfacial fluid dynamics induced by the effects of liquid-liquid/solid interface energy of the hybrid *LFS* will be investigated both experimentally and theoretically. In addition, I would also like to theoretically study the ion transport in the electrolyte flowing over *LFS* with nonhomogeneous surface charge density and interface energy. The streaming potential and energy conversion efficiency will also be experimentally measured and theoretically analyzed based on the ion transport behavior to provide theoretical guidance for designing electrokinetic power source. Besides the fundamental study of the underlying physics of nano electrokinetics on *LFS*, the practical nanoscale electrokinetics based power source will be developed and the energy conversion efficiency will be optimized based on the theoretical guidance to facilitate the practical application of electrokinetics.

Electricity harvesting through solar desalination process. A novel solar heat localization method using porous solar absorber has been used to enhance the evaporation efficiency. The aim has been to utilize solar energy in novel ways for water purification and desalination. Porous solar absorbers are usually composed by an array of micro/nano channels and EDL can form at the interface of salt water and solar absorber inner wall surfaces. Through nanoscale channels or tuning the surface charge density, only positive or negative ions can go through the channels. This charge separation process, which is similar to the working mechanism of electrokinetics, can prevent the formation of salt crystal and generate electricity

at the same time. Due to the imbalance of positive/negative ion concentration between the bottom and top sides of the porous solar absorber, the desalination system can generate electricity to harvest the electrokietic energy at the same time which would make better use of the incident solar energy.

References

(1) de Gennes, P.-G.; Brochard-Wyart, F.; Quere, D. *Capillarity and Wetting Phenomena: Drops, Bubbles, Pearls, Waves*; Springer: New York, NY, 2002.

(2) Kirby, B. J.; Hasselbrink, E. F. Zeta Potential of Microfluidic Substrates: 2. Data for Polymers. *Electrophoresis*. 2004, pp 203–213. https://doi.org/10.1002/elps.200305755.

(3) Lu, M. C.; Satyanarayana, S.; Karnik, R.; Majumdar, A.; Wang, C. C. A Mechanical-Electrokinetic Battery Using a Nano-Porous Membrane. *J. Micromechanics Microengineering* **2006**, *16* (4), 667–675. https://doi.org/10.1088/0960-1317/16/4/001.

(4) Roach, P.; Shirtcliffe, N. J.; Newton, M. I. Progess in Superhydrophobic Surface Development. *Soft Matter* **2008**, *4* (2), 224. https://doi.org/10.1039/b712575p.

(5) Papadopoulos, P.; Deng, X.; Vollmer, D.; Butt, H.-J. Electrokinetics on Superhydrophobic Surfaces. *J. Phys. Condens. Matter* **2012**, *24* (46), 464110. https://doi.org/10.1088/0953-8984/24/46/464110.

(6) Rothstein, J. P. Slip on Superhydrophobic Surfaces. *Annu. Rev. Fluid Mech.* **2010**, *42* (1), 89–109. https://doi.org/10.1146/annurev-fluid-121108-145558.

(7) Moreira, D.; Bandaru, P. R. Thermal Transport in Laminar Flow over Superhydrophobic Surfaces, Utilizing an Effective Medium Approach. *Phys. Fluids* **2015**, *27* (5), 052001. https://doi.org/10.1063/1.4919699.

(8) Kirby, B. J. Micro- and Nanoscale Fluid Mechanics: Transport in Microfluidic Devices. *Brian* **2010**, No. c, 512. https://doi.org/10.1007/s13398-014-0173-7.2.

(9) Moreira, D.; Park, S.; Lee, S.; Verma, N.; Bandaru, P. R. Dynamic Superhydrophobic Behavior in Scalable Random Textured Polymeric Surfaces. *J. Appl. Phys.* **2016**, *119* (12), 125302. https://doi.org/10.1063/1.4944472.

(10) Park, S.-H.; Lee, S.; Moreira, D.; Bandaru, P. R.; Han, I.; Yun, D.-J. Bioinspired Superhydrophobic Surfaces, Fabricated through Simple and Scalable Roll-to-Roll Processing. *Sci. Rep.* **2015**, *5*, 15430.

(11) Squires, T. M. Electrokinetic Flows over Inhomogeneously Slipping Surfaces. *Phys. Fluids* **2008**, *20* (9), 092105. https://doi.org/10.1063/1.2978954.

(12) Milne, A. J. B.; Amirfazli, A. The Cassie Equation: How It Is Meant to Be Used. *Adv. Colloid Interface Sci.* **2012**, *170*, 48–55.

(13) Liu, Y.; Moevius, L.; Xu, X.; Qian, T.; Yeomans, J. M.; Wang, Z. Pancake Bouncing on Superhydrophobic Surfaces. *Nat. Phys.* **2014**, *10*, 515–519.

(14) Chen, Y.; He, B.; Lee, J.; Patankar, N. A. Anisotropy in the Wetting of Rough Surfaces. *J. Colloid*

Interface Sci. **2005**, *281*, 458.

(15) Chung, J. Y.; Youngblood, J. P.; Stafford, C. M. Anisotropic Wetting on Tunable Micro-Wrinkled Surfaces. *Soft Matter* **2007**, *3*, 1163.

(16) Zhao, Y.; Lu, Q.; Li, M.; Li, X. Anisotropic Wetting Characteristics on Submicrometer-Scale Periodic Grooved Surface. *Langmuir* **2007**, *23*, 6212.

(17) Xia, D.; Brueck, S. R. J. Strongly Anisotropic Wetting on One-Dimensional Nanopattrened Surfaces. *Nanoletters* **2008**, *8*, 2819.

(18) Xia, D.; He, X.; Jiang, Y.-B.; Lopez, G. P.; Brueck, S. R. J. Tailoring Anisotropic Wetting Properties on Submicrometer-Scale Periodic Grooved Surfaces. *Langmuir* **2010**, *26*, 2700.

(19) Choi, W.; Tuteja, A.; Mabry, J. M.; Cohen, R. E.; Mckinley, G. H. A Modified Cassie–Baxter Relationship to Explain Contact Angle Hysteresis and Anisotropy on Non-Wetting Textured Surfaces. *J. Colloid Interface Sci.* **2009**, *339*, 208.

(20) Bocquet, L.; Lauga, E. A Smooth Future? *Nature Materials*. 2011, pp 334–337. https://doi.org/10.1038/nmat2994.

(21) Wilson, M. Superhydrophobic Surfaces Reduce Drag. *Phys. Today* **2009**, 16–18.

(22) Yong, J.; Yang, Q.; Chen, F.; Zhang, D.; Farooq, U.; Du, G.; Hou, X. A Simple Way to Achieve Superhydrophobicity, Controllable Water Adhesion, Anisotropic Sliding, and Anisotropic Wetting Based on Femtosecond-Laser-Induced Line-Patterned Surfaces. *J. Mater. Chem. A* **2014**, *2*, 5499–5507.

(23) DuPont Performance Lubricants-Applications for the Automotive Industry. *DuPont, Inc.* **2009**.

(24) Nowlin, T. E.; Foss Smith, D. Surface Characterization of Plasma-treated Poly-p-xylylene Films. *J. Appl. Polmer Sci.* **1980**, *25* (8), 1619.

(25) Israelachvili, J. N. *Intermolecular and Surface Forces,* 3rd ed.; Academic Press: San Diego, 2011.

(26) Mahadevan, L.; Pomeau, Y. Rolling Droplets. *Phys. Fluids* **1999**, *11*, 2449.

(27) Yao, X.; Hu, Y.; Grinthal, A.; Wong, T.-S.; Mahadevan, L.; Aizenberg, J. Adaptive Fluid-Infused Porous Films with Tunable Transparency and Wettability. *Nat. Mater.* **2013**, *12*, 529–534.

(28) Tsai, P.; Lammertink, R. G. H.; Wessling, M.; Lohse, D. Evaporation-Triggered Wetting Transition for Water Droplets upon Hydrophobic Microstructures. *Phys. Rev. Lett.* **2010**, *104*, 116102.

(29) Ybert, C.; Barentin, C.; Cottin-Bizonne, C.; Joseph, P.; Bocquet, L. Achieving Large Slip with Superhydrophobic Surfaces: Scaling Laws for Generic Geometries. *Phys. Fluids* **2007**, *19* (12). https://doi.org/10.1063/1.2815730.

(30) Lauga, E.; Stone, H. A. Effective Slip in Pressure-Driven Stokes Flow. *J. Fluid Mech.* **2003**, *489*, 55–77.

(31) Madou, M. *Fundamentals of Microfabrication* , 2nd ed.; CRC Press: Boca Raton, FL, 2002.

(32) Dukhin, S. S. Development of Notions as to the Mechanism of Electrokinetic Phenomena and Teh Structure of the Colloid Micelle. In *Surface and Colloid Science*; John Wiley & Sons: New York, NY, 1974; pp 1–47.

(33) Morrison, F. A.; Osterle, J. F. Electrokinetic Energy Conversion in Ultrafine Capillaries. *J. Chem. Phys.* **1965**, *43* (6), 2111–2115. https://doi.org/10.1063/1.1697081.

(34) Bahga, S. S.; Vinogradova, O. I.; Bazant, M. Z. Anisotropic Electro-Osmotic Flow over Super-Hydrophobic Surfaces. *J. Fluid Mech.* **2010**, *644*, 245–255.

(35) Squires, T. M. Electrokinetic Flows over Inhomogeneously Slipping Surfaces. *Phys. Fluids* **2008**, *20* (9), 092105. https://doi.org/10.1063/1.2978954.

(36) Kirby, B. J.; Hasselbrink, E. F. Zeta Potential of Microfluidic Substrates: 1. Theory, Experimental Techniques, and Effects on Separations. *Electrophoresis*. 2004, pp 187–202. https://doi.org/10.1002/elps.200305754.

(37) Whitesides, G. M. The Origins and the Future of Microfluidics. *Nature* **2006**, *442*, 368–373.

(38) Bard, A. J.; Faulkner, L. R. *Electrochemical Methods: Fundamentals and Applications*, 2nd ed.; John Wiley: New York, 2001.

(39) Hunter, R. J. *Zeta Potential in Colloid Science: Principles and Applications*; Academic Press: San Diego, CA, 1986.

(40) Kundu, P. K.; Cohen, I. M. *Fluid Mechanics*; 2008. https://doi.org/978-0-12-381399-2.

(41) Joly, L.; Ybert, C.; Trizac, E.; Bocquet, L. Hydrodynamics within the Electric Double Layer on Slipping Surfaces. *Phys. Rev. Lett.* **2004**, *93* (25), 257805. https://doi.org/10.1103/PhysRevLett.93.257805.

(42) Joseph, P.; Cottin-Bizonne, C.; Benoît, J. M.; Ybert, C.; Journet, C.; Tabeling, P.; Bocquet, L. Slippage of Water Past Superhydrophobic Carbon Nanotube Forests in Microchannels. *Phys. Rev. Lett.* **2006**, *97* (15). https://doi.org/10.1103/PhysRevLett.97.156104.

(43) Bouzigues, C. I.; Tabeling, P.; Bocquet, L. Nanofluidics in the Debye Layer at Hydrophilic and Hydrophobic Surfaces. *Phys. Rev. Lett.* **2008**, *101* (11), 114503. https://doi.org/10.1103/PhysRevLett.101.114503.

(44) Khair, A. S.; Squires, T. M. Surprising Consequences of Ion Conservation in Electro-Osmosis over a Surface Charge Discontinuity. *J. Fluid Mech.* **2008**, *615*, 323–334.

(45) Khair, A. S.; Squires, T. M. The Influence of Hydrodynamic Slip on the Electrophoretic Mobility

of a Spherical Colloidal Particle. *Phys. Fluids* **2009**, *21*, 042001.

(46) Van Der Heyden, F. H. J.; Bonthuis, D. J.; Stein, D.; Meyer, C.; Dekker, C. Electrokinetic Energy Conversion Efficiency in Nanofluidic Channels. *Nano Lett.* **2006**, *6* (10), 2232–2237. https://doi.org/10.1021/nl061524l.

(47) Wong, T.-S.; Kang, S. H.; Tang, S. K. Y.; Smythe, E. J.; Hatton, B. D.; Grinthal, A.; Aizenberg, J. Bioinspired Self-Repairing Slippery Surfaces with Pressure-Stable Omniphobicity. *Nature* **2011**, *477*, 443–447.

(48) Hou, X.; Li, J.; Tesler, A. B.; Yao, Y.; Wang, M.; Min, L.; Sheng, Z.; Aizenberg, J. Dynamic Air/Liquid Pockets for Guiding Microscale Flow. *Nat. Commun.* **2018**, *9* (1). https://doi.org/10.1038/s41467-018-03194-z.

(49) Schrott, W.; Slouka, Z.; Červenka, P.; Ston, J.; Nebyla, M.; Přibyl, M.; Šnita, D. Study on Surface Properties of PDMS Microfluidic Chips Treated with Albumin. *Biomicrofluidics* **2009**, *3* (4). https://doi.org/10.1063/1.3243913.

(50) Marinova, K. G.; Alargova, R. G.; Denkov, N. D.; Velev, O. D.; Petsev, D. N.; Ivanov, I. B.; Borwankar, R. P. Charging of Oil−water Interfaces Due to Spontaneous Adsorption of Hydroxyl Ions. *Langmuir* **1996**, *12* (8), 2045–2051. https://doi.org/10.1021/la950928i.

(51) Lo, H. W.; Tai, Y. C. Parylene-Based Electret Power Generators. *J. Micromechanics Microengineering* **2008**, *18* (10). https://doi.org/10.1088/0960-1317/18/10/104006.

(52) Thamida, S. K.; Chang, H.-C. Nonlinear Electrokinetic Ejection and Entrainment Due to Polarization at Nearly Insulated Edges. *Phys. Fluids* **2002**, *14*, 4315.

(53) Yossifon, G.; Frankel, I.; Miloh, T. On Electro-Osmotic Flows through Microchannel Junctions. *Phys. Fluids* **2006**, *18* (11). https://doi.org/10.1063/1.2391701.

(54) Zhao, H. Streaming Potential Generated by a Pressure-Driven Flow over Superhydrophobic Stripes. *Phys. Fluids* **2011**, *23* (2), 022003. https://doi.org/10.1063/1.3551616.

(55) Ng, C. O.; Chu, H. C. W. Electrokinetic Flows through a Parallel-Plate Channel with Slipping Stripes on Walls. *Phys. Fluids* **2011**, *23* (10), 102002. https://doi.org/10.1063/1.3647582.

(56) Yang, D.; Kwok, D. Y. Analytical Tretament of Flow in Infinitely Extended Circular Microchannels and the Effect of Slippage to Increase Flow Efficiency. *J. Micromechanics Microengineering* **2003**, *13*, 115.

(57) Lyklema, J.; Overbeek, J. T. G. On the Interpretation of Electrokinetic Potentials. *J. Colloid Sci.* **1961**, *16*, 501–512.

(58) Wu, P.; Qio, R. Physical Origins of Apparently Enhanced Viscosity of Interfacial Fluids in Electrokinetic Transport. *Phys. Fluids* **2011**, *23*, 072005.

(59) Li, P. C.; Harrison, D. J. Transport, Manipulation, and Reaction of Biological Cells on-Chip Using

Electrokinetic Effects. *Anal. Chem.* **1997**, *69* (8), 1564–1568. https://doi.org/10.1021/ac9606564.

(60) Jacobson, S. C.; McKnight, T. E.; Ramsey, J. M. Microfluidic Devices for Electrokinetically Driven Parallel and Serial Mixing. *Anal. Chem.* **1999**, *71* (20), 4455–4459. https://doi.org/10.1021/ac990576a.

(61) Zhang, R.; Wang, S.; Yeh, M. H.; Pan, C.; Lin, L.; Yu, R.; Zhang, Y.; Zheng, L.; Jiao, Z.; Wang, Z. L. A Streaming Potential/Current-Based Microfluidic Direct Current Generator for Self-Powered Nanosystems. *Adv. Mater.* **2015**, *27* (41), 6482–6487. https://doi.org/10.1002/adma.201502477.

(62) Van Der Heyden, F. H. J.; Bonthuis, D. J.; Stein, D.; Meyer, C.; Dekker, C. Power Generation by Pressure-Driven Transport of Ions in Nanofluidic Channels. *Nano Lett.* **2007**, *7* (4), 1022–1025. https://doi.org/10.1021/nl070194h.

(63) Xie, Y.; Sherwood, J. D.; Shui, L.; van den Berg, A.; Eijkel, J. C. T. Strong Enhancement of Streaming Current Power by Application of Two Phase Flow. *Lab Chip* **2011**, *11* (23), 4006. https://doi.org/10.1039/c1lc20423h.

(64) Xie, Y.; Wang, X.; Xue, J.; Jin, K.; Chen, L.; Wang, Y. Electric Energy Generation in Single Track-Etched Nanopores. *Appl. Phys. Lett.* **2008**, *93* (16). https://doi.org/10.1063/1.3001590.

(65) Li, Z.; Liu, Y.; Zheng, Y.; Xu, R. Zeta Potential at the Root Surfaces of Rice Characterized by Streaming Potential Measurements. *Plant Soil* **2015**, *386* (1–2), 237–250. https://doi.org/10.1007/s11104-014-2259-6.

(66) Ren, Y.; Stein, D. Slip Enhanced Electrokinetic Energy Conversion in Nanofluidic Channels. *Nanotechnology* **2008**, *19*, 195707.

(67) Yamada, H.; Bandaru, P. R. Enhanced Electrical Current Densities in Electrochemical Systems through the Use of Nanostructured Electrodes. *Appl. Phys. Lett.* **2014**, *104* (21), 213901. https://doi.org/10.1063/1.4879837.

(68) Van Der Heyden, F. H. J.; Stein, D.; Dekker, C. Streaming Currents in a Single Nanofluidic Channel. *Phys. Rev. Lett.* **2005**, *95* (11), 116104. https://doi.org/10.1103/PhysRevLett.95.116104.

(69) Electrokinetic Microchannel Battery by Means of Electrokinetic and Microfluidic Phenomena. *news@nature* **2003**. https://doi.org/10.1038/news031020-4.

(70) Zhu, Y.; Granick, S. Limits of the Hydrodynamic No-Slip Boundary Condition. *Phys. Rev. Lett.* **2002**, *88*, 106102.

(71) Cottin-Bizonne, C.; Cross, B.; Steinbeger, A.; Charlaix, E. Boundary Slip on Smooth Hydrophobic Surfaces: Intrinsic Effects and Possible Artifacts. *Phys. Rev. Lett.* **2005**, *94*, 056102.

(72) Goda, T.; Konno, T.; Takai, M.; Ishihara, K. Photoinduced Phospholipid Polymer Grafting on Parylene Film: Advanced Lubrication and Antibiofouling Properties. *Colloids Surfaces B Biointerfaces* **2007**, *54* (1), 67–73. https://doi.org/10.1016/j.colsurfb.2006.09.006.

(73) Beattie, J. K. The Intrinsic Charge on Hydrophobic Microfluidic Substrates. *Lab Chip* **2006**, *6* (11), 1409. https://doi.org/10.1039/b610537h.

(74) Marinova, K. G.; Alargova, R. G.; Denkov, N. D.; Velev, O. D.; Petsev, D. N.; Ivanov, I. B.; Borwankar, R. P. Charging of Oil−Water Interfaces Due to Spontaneous Adsorption of Hydroxyl Ions. *Langmuir* **1996**, *12* (8), 2045–2051. https://doi.org/10.1021/la950928i.

(75) Probstein, R. F. *Physicochemical Hydrodynamics: An Introduction*; John Wiley & Sons Inc.: New York, 1994.

(76) Bard, A. J.; Faulkner, L. R. *Electrochemical Methods: Fundamentals and Applications, 2nd Ed.*; 2001.

(77) Jackson, J. D. *Classical Electrodynamics*; John Wiley: New York, 1999.

(78) Rothstein, J. P. Slip on Superhydrophobic Surfaces. *Annu. Rev. Fluid Mech.* **2010**, *42* (1), 89–109. https://doi.org/10.1146/annurev-fluid-121108-145558.

(79) van der Heyden, F. H. J.; Bonthuis, D. J.; Stein, D.; Meyer, C.; Dekker, C. Power Generation by Pressure-Driven Transport of Ions in Nanofluidic Channels. *Nanoletters* **2007**, *7*, 1022–1025.

(80) Xie, Y.; Sherwood, J. D.; Shui, L.; van den Berg, A.; Eijkel, J. C. T. Strong Enhancement of Streaming Current Power by Application of Two Phase Flow. *Lab Chip* **2011**, *11*, 4005–4011.

(81) Xie, Y.; Wang, X.; Xue, J.; Jin, K.; Chen, L.; Wang, Y. Electric Energy Generation in Single Track-Etched Nanopores. *Appl. Phys. Lett.* **2008**, *93*, 163116.

(82) Li, Z.-Y.; Liu, Y.; Zheng, Y.-Y.; Xu, R.-K. Zeta Potential at the Root Surfaces of Rice Characterized by Streaming Potential Measurements. *Plant Soil* **2015**, *386*, 237–250.

(83) Yang, J.; Lu, F.; Kostiuk, L. W.; Kwok, D. Y. Electrokinetic Microchannel Battery by Means of Electrokinetic and Microfluidic Phenomena. *J. Micromechanics Microengineering* **2003**, *13* (6), 963–970. https://doi.org/10.1088/0960-1317/13/6/320.

(84) Olthuis, W.; Schippers, B.; Eijkel, J.; Van Den Berg, A. Energy from Streaming Current and Potential. *Sensors Actuators, B Chem.* **2005**, *111–112* (SUPPL.), 385–389. https://doi.org/10.1016/j.snb.2005.03.039.

(85) Pennathur, S.; Eijkel, J. C. T.; van de Berg, A. Energy Conversion in Microsystems: Is There a Role for Micro/Nanofluidics? *Lab Chip* **2007**, *7*, 1234–1237.

(86) Hunter, R. J. *Foundations of Colloid Science*; Oxford University Press: Oxford, UK, 2001.

(87) Morrison Jr., F. A.; Osterle, J. F. Electrokinetic Energy Conversion in Ultrafine Capillaries. *J. Chem. Phys.* **1965**, *43*, 2111.

(88) Quincke, G. Ueber Eine Neue Art Elektrischer Ströme. *Ann. der Phys. und Chemie* **1859**, *183* (5), 1–47. https://doi.org/10.1002/andp.18591830502.

(89) Daiguji, H.; Yang, P.; Szeri, A. J.; Majumdar, A. Electrochemomechanical Energy Conversion in Nanofluidic Channels. *Nano Lett.* **2004**, *4* (12), 2315–2321. https://doi.org/10.1021/nl0489945.

(90) Zhang, X.; Tartakovsky, D. M. Effective Ion Diffusion in Charged Nanoporous Materials. *J. Electrochem. Soc.* **2017**, *164*, E53–E61.

(91) Battiato, I. Effective Medium Theory for Drag-Reducing Micro-Patterned Surfaces in Turbulent Flows. *Eur. Phys. J. , E* **2014**, *37*, 19.

(92) Battiato, I.; Bandaru, P. R.; Tartakovsky, D. M. Elastic Response of Carbon Nanotube Forests to Aerodynamic Stresses. *Phys. Rev. Lett.* **2010**, *105* (14). https://doi.org/10.1103/PhysRevLett.105.144504.

(93) Joly, L.; Ybert, C.; Trizac, E.; Bocquet, L. Hydrodynamics within the Electric Double Layer on Slipping Surfaces. *Phys. Rev. Lett.* **2004**, *93*, 257805.

(94) Squires, T. M. Electrokinetic Flows over Inhomogeneously Slipping Surfaces. *Phys. Fluids* **2008**, *20* (9), 092105. https://doi.org/10.1063/1.2978954.

(95) Bahga, S. S.; Vinogradova, O. I.; Bazant, M. Z. Anisotropic Electro-Osmotic Flow over Super-Hydrophobic Surfaces. *J. Fluid Mech.* **2010**, *644*, 245–255. https://doi.org/10.1017/S0022112009992771.

(96) Zhao, H. Electro-Osmotic Flow over a Charged Superhydrophobic Surface. *Phys. Rev. E - Stat. Nonlinear, Soft Matter Phys.* **2010**, *81* (6), 066314. https://doi.org/10.1103/PhysRevE.81.066314.

(97) Steffes, C.; Baier, T.; Hardt, S. Enabling the Enhancement of Electroosmotic Flow over Superhydrophobic Surfaces by Induced Charges. *Colloids Surfaces A Physicochem. Eng. Asp.* **2011**, *376* (1–3), 85–88. https://doi.org/10.1016/j.colsurfa.2010.09.002.

(98) Fan, B.; Bhattacharya, A.; Bandaru, P. R. Enhanced Voltage Generation through Electrolyte Flow on Liquid-Filled Surfaces. *Nat. Commun.* **2018**, *9*, 4050.

(99) Sun, R.; Ng, C. O. Effective Slip for Flow through a Channel Bounded by Lubricant-Impregnated Grooved Surfaces. *Theor. Comput. Fluid Dyn.* **2017**, *31* (2), 189–209. https://doi.org/10.1007/s00162-016-0414-9.

(100) Schönecker, C.; Hardt, S. Assessment of Drag Reduction at Slippery, Topographically Structured Surfaces. *Microfluid. Nanofluidics* **2015**, *19* (1), 199–207. https://doi.org/10.1007/s10404-015-1565-5.

(101) Solomon, B. R.; Khalil, K. S.; Varanasi, K. K. Drag Reduction Using Lubricant-Impregnated Surfaces in Viscous Laminar Flow. *Langmuir* **2014**, *30* (36), 10970–10976. https://doi.org/10.1021/la5021143.

(102) Wong, T.-S.; Kang, S. H.; Tang, S. K. Y.; Smythe, E. J.; Hatton, B. D.; Grinthal, A.; Aizenberg, J. Bioinspired Self-Repairing Slippery Surfaces with Pressure-Stable Omniphobicity. *Nature* **2011**, *477* (7365), 443–447. https://doi.org/10.1038/nature10447.

(103) Schonecker, C.; Baier, T.; Hardt, S. Influence of the Enclosed Fluid on the Flow over a Microstructured Surface in the Cassie State. *J. Fluid Mech.* **2014**, *740* (1), 168–195. https://doi.org/10.1017/jfm.2013.647.

(104) Schönecker, C.; Hardt, S. Longitudinal and Transverse Flow over a Cavity Containing a Second Immiscible Fluid. *J. Fluid Mech.* **2013**, *717*, 376–394. https://doi.org/10.1017/jfm.2012.577.

(105) Fan, B.; Bandaru, P. R. Anisotropy in the Hydrophobic and Oleophilic Characteristics of Patterned Surfaces. *Appl. Phys. Lett.* **2017**, *111* (26), 261603. https://doi.org/10.1063/1.5000540.

(106) Howell, C.; Vu, T. L.; Johnson, C. P.; Hou, X.; Ahanotu, O.; Alvarenga, J.; Leslie, D. C.; Uzun, O.; Waterhouse, A.; Kim, P.; et al. Stability of Surface-Immobilized Lubricant Interfaces under Flow. *Chem. Mater.* **2015**, *27*, 1792–1800.

(107) Bazant, M. Z.; Vinogradova, O. I. Tensorial Hydrodynamic Slip. *J. Fluid Mech.* **2008**, *613*, 125.

(108) Livescu, D.; Ristorcelli, J. R. Buoyancy-Driven Variable-Density Turbulence. *J. Fluid Mech.* **2007**, *591*, 43–71. https://doi.org/10.1017/S0022112007008270.

(109) Maduar, S. R.; Belyaev, A. V.; Lobaskin, V.; Vinogradova, O. I. Electrohydrodynamics near Hydrophobic Surfaces. *Phys. Rev. Lett.* **2015**, *114*, 118301.

(110) Kundu, P. K.; Cohen, I. M. Front Matter BT - Fluid Mechanics. *Fluid Mech.* **2008**, No. 0.

(111) Kumar, D.; Singh, A.; Tarsikka, P. S. Interrelationship between Viscosity and Electrical Properties for Edible Oils. **2013**, *50* (June), 549–554. https://doi.org/10.1007/s13197-011-0346-8.

(112) Belyaev, A. V.; Vinogradova, O. I. Effective Slip in Pressure-Driven Flow Past Super-Hydrophobic Stripes. *J. Fluid Mech.* **2010**, *652*, 489.

(113) Nizkaya, T. V.; Asmolov, E. S.; Vinogradova, O. I. Gas Cushion Model and Hydrodynamic Boundary Conditions for Superhydrophobic Textures. *Phys. Rev. E* **2014**, *90*, 043017.

(114) Belyaev, A. V.; Vinogradova, O. I. Electro-Osmosis on Anisotropic Superhydrophobic Surfaces. *Phys. Rev. Lett.* **2011**, *107*, 098301.

(115) Brunet, E.; Ajdari, A. Generalized Onsager Relations for Electrokinetic Effects in Anisotropic and Heterogenous Geometries. *Phys. Rev. E* **2004**, *69*, 016306.

(116) Asmolov, E. S.; Nizkaya, T. V.; Vinogradova, O. I. Enhanced Slip Properties of Lubricant-Infused Grooves. *Phys. Rev. E* **2018**, *98*, 033103.

(117) Zhao, H. Electro-Osmotic Flow over a Charged Superhydrophobic Surface. *Phys. Rev. E* **2010**, *81*, 066314.

(118) Schmidt, W. F.; Yoshino, K. Ion Mobilities in Non-Polar Dielectric Liquids: Silicone Oils. *IEEE Trans. Dielectr. Electr. Insul.* **2015**, *22*, 2424–2427.

(119) Choi, C.-H.; Kim, C.-J. Large Slip of Aqueous Liquid Flow over a Nanoengineered Superhydrophobic Surface. *Phys. Rev. Lett.* **2006**, *96*, 066001.

(120) Pascall, A. J.; Squires, T. M. Electrokinetics at Liquid/Liquid Interfaces. *J. Fluid Mech.* **2011**, *684*, 163–191. https://doi.org/10.1017/jfm.2011.288.

(121) Zhang, R.; Wang, S.; Yeh, M.-H.; Pan, C.; Lin, L.; Yu, R.; Zhang, Y.; Zheng, L.; Jiao, Z.; Wang, Z. L. A Streaming Potential/Current-Based Microfluidic Direct Current Generator for Self-Powered Nanosystems. *Adv. Mater.* **2015**, *27*, 6482–6487.

(122) Wexler, J. S.; Grosskopf, A.; Chow, M.; Fan, Y.; Jacobi, I.; Stone, H. A. Robust Liquid-Infused Surfaces through Patterned Wettability. *Soft Matter* **2015**, *11*, 5023.

(123) Sadullah, M. S.; Semprebon, C.; Kusumaatmaja, H. Drop Dynamics on Liquid Infused Surfaces: The Role of the Wetting Ridge. **2018**. https://doi.org/10.1021/acs.langmuir.8b01660.

(124) Bahga, S. S.; Vinogradova, O. I.; Bazant, M. Z. Anisotropic Electro-Osmotic Flow over Super-Hydrophobic Surfaces. *J. Fluid Mech.* **2010**, *644*, 245–255. https://doi.org/10.1017/S0022112009992771.

(125) Fan, B.; Bandaru, P. R. Modulation of the Streaming Potential and Slip Characteristics in Electrolyte Flow over Liquid-Filled Surfaces. *Langmuir* **2019**, *35* (18), 6203–6210. https://doi.org/10.1021/acs.langmuir.9b00704.

(126) Nizkaya, T. V.; Asmolov, E. S.; Zhou, J.; Schmid, F.; Vinogradova, O. I. Flows and Mixing in Channels with Misaligned Superhydrophobic Walls. *Phys. Rev. E* **2015**, *91*, 033020.

(127) Wexler, J. S.; Jacobi, I.; Stone, H. A. Shear-Driven Failure of Liquid-Infused Surfaces. *Phys. Rev. Lett.* **2015**, *114* (16), 1–5. https://doi.org/10.1103/PhysRevLett.114.168301.

(128) Ajdari, A. Transverse Electrokinetic and Microfluidic Effects in Micropatterned Channels: Lubrication Analysis for Slab Geometries. *Phys. Rev. E - Stat. Physics, Plasmas, Fluids, Relat. Interdiscip. Top.* **2002**, *65* (1), 1–9. https://doi.org/10.1103/PhysRevE.65.016301.

(129) Bazant, M. Z.; Vinogradova, O. I. Tensorial Hydrodynamic Slip. *J. Fluid Mech.* **2008**, *613*, 125–134. https://doi.org/10.1017/S002211200800356X.

(130) Vemuri, K. P.; Bandaru, P. R. Geometrical Considerations in the Control and Manipulation of Conductive Heat Flux in Multilayered Thermal Metamaterials. *Appl. Phys. Lett.* **2013**, *103* (13), 133111. https://doi.org/10.1063/1.4823455.

(131) Stroock, A. D.; Dertinger, S. K.; Whitesides, G. M.; Ajdari, A. Patterning Flows Using Grooved Surfaces. *Anal. Chem.* **2002**, *74* (20), 5306–5312. https://doi.org/10.1021/ac0257389.